FRONTIERS OF PHYSICS

RESEARCH ARTICLE
Volume 17 / Issue 6 / 62504 / 2022

Fast topological pumping for the generation of large-scale Greenberger–Horne–Zeilinger states in a superconducting circuit

Jin-Xuan Han[1], Jin-Lei Wu[2,†], Zhong-Hui Yuan[1], Yan Xia[3], Yong-Yuan Jiang[1,4,5,6], Jie Song[1,4,5,6,‡]

1 School of Physics, Harbin Institute of Technology, Harbin 150001, China
2 Department of Optoelectronics Science, Harbin Institute of Technology, Weihai 264209, China
3 Department of Physics, Fuzhou University, Fuzhou 350002, China
4 Collaborative Innovation Center of Extreme Optics, Shanxi University, Taiyuan 030006, China
5 Key Laboratory of Micro-Nano Optoelectronic Information System, Ministry of Industry and Information Technology, Harbin 150001, China
6 Key Laboratory of Micro-Optics and Photonic Technology of Heilongjiang Province, Harbin Institute of Technology, Harbin 150001, China
Corresponding authors. E-mail: †jinlei_wu@126.com, ‡jsong@hit.edu.cn
Received April 21, 2022; accepted July 25, 2022

ABSTRACT

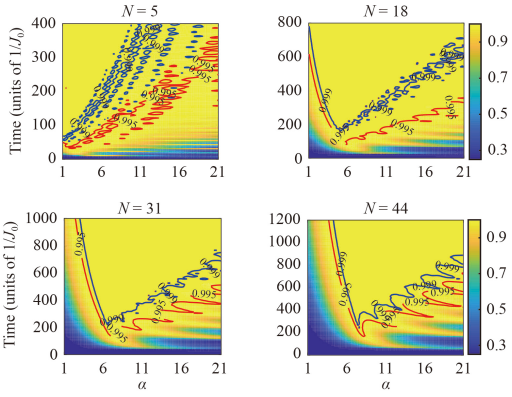

Topological pumping of edge states in the finite lattice with nontrivial topological phases provides a powerful means for robust excitation transfer, requiring extremely slow evolution to follow an adiabatic transfer. Here, we propose fast topological pumping via edge channels to generate large-scale Greenberger–Horne–Zeilinger (GHZ) states in a topological superconducting circuit with a sped-up evolution process. The scheme indicates a conceptual way of designing fast topological pumping related to the instantaneous energy spectrum characteristics rather than relying on the shortcuts to adiabaticity. Based on fast topological pumping, large-scale GHZ states show greater robustness against on-site potential defects, the fluctuation of couplings and losses of the system in comparison with the conventional adiabatic topological pumping. With experimentally feasible qutrit-resonator coupling strengths and moderate decay rates of qutrits and resonators, fast topological pumping drastically improves the scalability of GHZ states with a high fidelity. Our work opens up prospects for the realization of large-scale GHZ states based on fast topological pumping in the superconducting quantum circuit system, which provides potential applications of topological matters in quantum information processing.

Keywords topological pumping, superconducting ciruit, large-scale, Greenberger–Horne–Zeilinger states

1 Introduction

Topological phenomena, rooted in global geometric properties characterized by topological invariants, provide natural protection against perturbation and disorder in systems [1, 2]. Topological quantum pumping serves as a transport phenomenon making use of topological properties of a modulated system, including two types: Thouless pumping via topological bulk bands [3, 4] and adiabatic pumping via topological edge modes [5–11].

Higher Education Press

https://doi.org/10.1007/s11467-022-1193-y

Thouless pumping is a quantized transport directly connected to the Chern number [4]. In the adiabatic pumping, the edge state at one side will be adiabatically coupled to bulk states and then transferred to the other side [5–11]. On account of a topological nature, the transport scheme demonstrates to be robust against the disorder, exploiting topological pumping greatly concerned in applications such as quantum state transfer [8, 12, 13], quantum information processing [14] and quantum entanglement [15].

A very promising direction towards the realization of an efficient platform to perform fault-tolerant quantum computation combines topological states of matter with superconducting circuits [16–19]. One of the most appealing properties of topological systems is that they host edge states, which are robust to different sources of quantum decoherence. Superconducting quantum circuits with high coherence and straightforward connectivity can be fabricated with well-designed parameters and be accessible to manufacture tens of qubits with various types of couplings [20–25], which enables to implement large-scale quantum simulation [26–30]. Recently, such state-of-the-art techniques enable superconducting quantum circuits to be a promising candidate for investigating topological phenomena theoretically and experimentally [31–47]. Topical examples include analogies to topological quantum walks [39], Zak phases [40], topological phase transitions [41, 42], Chern numbers [43, 44], topological Uhlmann phase [47] and topological magnon insulator states [46] realizing in the phase space of microwave resonators and superconducting qubit, respectively. Furthermore, the topological robustness of anyonic braiding statistics has also been demonstrated in the superconducting quantum circuit [45].

So far, many topological states and effects have been implemented for quantum entanglement, which is pivotal for quantum communication, quantum information process and quantum metrology [48–50]. It has demonstrated the topological protected entangled $N00N$ state and its transport via edge states in Refs. [51–53]. The adiabatic topological pumping based on edge channels offered a topologically protected way to observe the Hong–Ou–Mandel interference [54] of a photon pair and generate spatial entangled states [9]. Additionally, large-scale Greenberger–Horne–Zeilinger (GHZ) states have been realized by adiabatic topological pumping via edge channels in a superconducting quantum system [15]. Nevertheless, the speed of procedures is extremely slow for a large-scale system, which is intrinsically limited by adiabatic requirements to avoid nonadiabatic transitions between the edge channel and the bulk bands. In order to refrain from the decoherence effects in the system, several proposals have been proposed to accelerate the process of quantum state transfer in topologically nontrivial systems [11–13, 55, 56]. The fast and robust quantum state transfer can be realized by performing shortcut-to-adiabaticity techniques [13]. A scheme of topological pumping based on adiabatic passage has been proposed by interfacing two dimerized Su–Schrieffer–Heeger (SSH) chains with different topological order [11, 56]. In the topological protected quantum state transfer, optimization techniques have been controlled to reach high-fidelity values for short evolution times [12, 55]. However, it is also urgent to improve the transfer efficiency in adiabatic topological pumping for generating large-scale entangled states, thereby making sense to enhance the robustness against decoherence effects [57–59] and random fluctuations from quantum system [60–62], and improve the feasibility and scalability of experimental implementations in quantum information processing [63–65].

GHZ state is a typical type of maximally entangled states, which is not only of great interest for fundamental tests of quantum mechanics [66], but also has applications in quantum communications [67, 68], error-correction protocols [69], quantum metrology [70] and high-precision spectroscopy [71]. The capability of entangling multiple particles is central to fundamental tests of quantum theory and the prerequisite for quantum information processing. During the past years, theoretical proposals of GHZ states have been investigated in circuit-QED system and other physical platform [15, 72–83]. Moreover, experimental realizations of entanglement of three superconducting qubits [84], and GHZ states with three superconducting qubits in circuit-QED system [85], five superconducting qubits via capacitance coupling [86], ten qubits connecting to a bus resonator in a superconducting circuit [87] and eighteen qubits in a 20-qubit superconducting device [25] have been reported. Furthermore, high-dimensional GHZ state with three superconducting transmon qutrits has also generated by the fidelity of $76\% \pm 1\%$ in a superconducting quantum processor [88]. However, the fidelity of GHZ states is limited by the ubiquitous noise and device imperfections based on the superconducting circuit system, indicating that the effectiveness of theoretical proposals and experimental realizations remains to be solved.

In this paper, we present a scheme of fast topological pumping via edge channels with respect to a single-excitation quantum state for generating large-scale GHZ states in a generalized SSH model of superconducting qutrit-resonator circuit. We analytically derive that such a generalized SSH model can be expressed as a two-band structure in momentum space, and its topologically trivial and nontrivial phases can be characterized by the Zak phases equal to 0 and π, respectively. The odd-size generalized SSH model is always in the topological nontrivial case, proved by the topologically protected zero-mode edge state in the energy spectrum. The scheme indicates a conceptual way of designing fast topological pumping depending on the instantaneous energy spectrum characteristics for speeding up the generation of large-scale GHZ states, which abides by the adiabatic passage. Furthermore, large-scale GHZ states are robust against

on-site potential defects, the fluctuation of couplings and losses of the system which are benefit from the chiral symmetry and topological property of system. Our work may facilitate potential applications of optimization techniques to control topological superconducting circuit system in quantum information processing, due to the following advantages and interests. Firstly, this work focuses on crucial aspects of the energy spectrum to design topological pumping in order to substantially speed up the evolution process, which does not rely on the shortcuts to adiabaticity [89, 90]. Secondly, the present scheme shows greater robustness and wider scalability for generating large-scale GHZ states than that in Ref. [15], owing to the fast topological pumping via edge channels. Finally, our method shows more simplicity and feasibility in the generalized SSH model confining to engineer nearest-neighbor couplings in comparison with introducing next-to-nearest-neighbor interactions in Ref. [13].

2 Physical model and engineering of topological pumping

2.1 Generalized SSH model and Zak phase

The schematic of our generalized SSH model is shown in Fig. 1(a), which describes a one-dimensional coupled superconducting qutrit-resonator chain and composes of N qutrits and N resonators, respectively. Each flux qutirt holds a three-level structure, forming two ground states $|L\rangle, |R\rangle$ and one excited state $|e\rangle$. The frequency of a single-mode resonator B_n is set to match resonantly with the transition frequency of $|L\rangle \leftrightarrow |e\rangle$ ($|R\rangle \leftrightarrow |e\rangle$) of the two nearest-neighbor qutrits A_n and A_{n+1}, when n is odd (even). Between two adjacent cells, the resonator

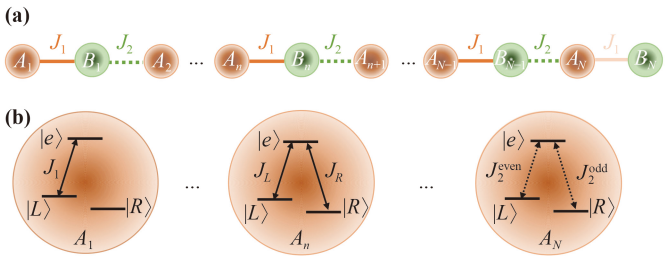

Fig. 1 **(a)** The diagrammatic sketch of a topological superconducting qutrit-resonator chain with the size of $2N$. The chain belongs to an SSH model whose n-th unit cell contains one flux qutrit A_n and one single-mode resonator B_n. The intra-cell and inter-cell coupling strengths are J_1 and J_2, respectively. **(b)** Schematics of energy level transitions for qutrits A_1, A_n $(1 < n < N)$, and A_N. The energy level structure of a flux qutrit holds two ground states ($|L\rangle$ and $|R\rangle$) and one excited state ($|e\rangle$). The coupling strengths between the resonator B_n and the qutrit A_n (A_{n+1}) is $J_L = J_1$ ($J_R = J_2$) when n is odd, or $J_L = J_2$ ($J_R = J_1$) when n is even.

B_n is coupled to its front qutrit A_n and the behind qutrit A_{n+1} with alternating coupling strengths J_1 and J_2, respectively. The interaction of the chain can be described by the following interaction-picture Hamiltonian ($\hbar = 1$)

$$H_I = \sum_n \left(J_1|e\rangle_n\langle j_n| + J_2|e\rangle_{n+1}\langle j_n|\right)b_n + \text{H.c.}, \tag{1}$$

where $j_n = L\ (R)$ when n is odd (even), and b_n the annihilation operator of the resonator B_n. Further, the one-dimensional coupled superconducting qutrit-resonator chain is analogous to an SSH model, which can be simplified as

$$H_I = \sum_n J_1 b_n S_n^\dagger + J_2 b_n S_{n+1}^\dagger + \text{H.c.}, \tag{2}$$

where $S_n^\dagger = |e\rangle_n\langle R|(\sigma_n^x)^n$ and $\sigma_n^x = |L\rangle_n\langle R| + |R\rangle_n\langle L|$. The operator $(\sigma_n^x)^n$ works for two different transitions $|L\rangle \leftrightarrow |e\rangle$ and $|R\rangle \leftrightarrow |e\rangle$ for qutrit A_n depending on the odevity of n.

For periodic boundary conditions, we can use the Bloch theorem and rewrite H_I as

$$H_I = \sum_{k_n \equiv \frac{2\pi n}{a_0}} \Psi_{k_n}^\dagger \mathcal{H}^B(k_n)\Psi_{k_n}, \quad -\frac{N}{2} < n < \frac{N}{2}, \tag{3}$$

with $\Psi_{k_n}^\dagger = (\psi_{S,k}^\dagger, \psi_{B,k}^\dagger) = N^{-1/2}\sum_{n=1}^N \mathrm{e}^{\mathrm{i}a_0 nk}(S_n^\dagger, b_n)$ and

$$\mathcal{H}^B(k) = J_2 \begin{pmatrix} 0 & \rho(k) \\ \rho^*(k) & 0 \end{pmatrix}, \tag{4}$$

where $\rho(k) = J_1/J_2 + \mathrm{e}^{-\mathrm{i}ka_0}$ with $k \in [-\pi/a_0, \pi/a_0]$. Introducing the vector of Pauli matrices $\sigma = (\sigma_x, \sigma_y)$, the Hamiltonian can be expressed in the form $\mathcal{H}^B(k) = -J_2\boldsymbol{g}(k)\cdot\sigma$ with $\boldsymbol{g}(k) = (\mathrm{Re}(\rho), -\mathrm{Im}(\rho))$. The eigenvalues can be obtained by diagonalizing $\mathcal{H}^B(k)$,

$$\epsilon_{k,\pm} = \pm J_2|\boldsymbol{g}(k)| = \pm J_2|\rho(k)| = \pm\sqrt{J_1^2 + J_2^2 + \cos(ka_0)}. \tag{5}$$

The corresponding eigenstates are

$$u_\pm(k) = \frac{1}{\sqrt{2}} \begin{pmatrix} \mathrm{e}^{-\mathrm{i}\phi(k)} \\ \pm 1 \end{pmatrix}, \tag{6}$$

where the phase $\phi(k)$ is given by $\cot\phi(k) = \frac{J_1/J_2}{\sin ka_0} + \cot ka_0$. Analyzing Eqs. (5) and (6), the eigenenergy spectrum of the system is divided into two bands, i.e., the negative eigenenergy band $u_-(k)$ and positive eigenenergy band $u_+(k)$. This model belongs to the BDI class according to the standard topological classification [91] and possesses two topological distinct phases for $J_1 < J_2$ and $J_1 > J_2$, where the band gap is closed at the boundaries of the first Brillouin zone ($k = \pm\pi/a_0$). The chain is more like a "conductor" when the system lies in the phase transition point at $J_1 = J_2$. Otherwise, the chain behaves as an "insulator". However, there exists a band gap with

width $2|J_1 - J_2|$ except for the closed points. It is noted that the trajectory of the vector $\boldsymbol{g}(k)$ for all k enclose or does not enclose the origin and $|\phi(k)| \in [0, 2\pi]$ or $|\phi(k)| < \pi/2$ when $J_1 < J_2$ or $J_1 > J_2$. This topological behavior of the phase $\phi(k)$ is bound up with the value of the Zak phase, given by

$$\mathcal{Z} = \mathrm{i}\int_{-\pi/a}^{\pi/a} \mathrm{d}k[u_-^{\dagger}(k)\partial_k u_-(k)] = \frac{1}{2}\oint \mathrm{d}k\frac{\mathrm{d}\phi}{\mathrm{d}k} = \frac{\Delta\phi}{2}, \tag{7}$$

where $\Delta\phi$ is the variation of $\phi(k)$ when k varies across the full Brillouin zone. After some algebra, one can obtain $\mathcal{Z} = \pi$ and $\mathcal{Z} = 0$ for the cases of $J_1 < J_2$ and $J_1 > J_2$, respectively. The winding of the vector $\boldsymbol{g}(k)$ when k varies across the Brillouin zone is shown in Figs. 2(a) and (b) for two values of $J_1/J_2 < 1$ and $J_1/J_2 > 1$, respectively. When $J_1/J_2 < 1$, the loop encloses the origin and the phase $\phi(k)$ can take an any value. As for $J_1/J_2 > 1$, the curve $\boldsymbol{g}(k)$ does not enclose the origin and $|\phi(k)| < \pi/2$ for all k. Thus, topological phenomenon of the phase $\phi(k)$ is related to the value of Zak phase. The Zak phase $\mathcal{Z}$ is π times the winding number of the curve $\boldsymbol{g}(k)$ around the origin and is, therefore, zero if this curve does not enclose the origin while π if it does. Accordingly,

$$\begin{aligned} &\mathcal{Z} = \pi \quad \text{when} \quad J_1/J_2 < 1, \\ &\mathcal{Z} = 0 \quad \text{when} \quad J_1/J_2 > 1. \end{aligned} \tag{8}$$

The results show that tuning the ratio J_1/J_2 induces a topological phase transition characterized by the Zak phase.

2.2 Analaysis of fast topological pumping and edge state

As for even- and odd-sized SSH chains, the characteristics of energy spectrum versus the varying J_1/J_2 demonstrate the different distribution of zero energy mode [92]. Under the open boundary condition for the even-sized SSH chain, the two phases are distinguished by the presence and absence of degenerate zero-mode edge states with topologically nontrivial phase $J_1/J_2 < 1$ and topologically trivial phase $J_1/J_2 > 1$, as shown in Fig. 2(c). As expected in Fig. 2(d), there is only one topologically protected zero-mode edge state in the band gap with regardless to the value of J_1/J_2. Therefore, the odd-sized chain is always in the topological nontrivial phase [93].

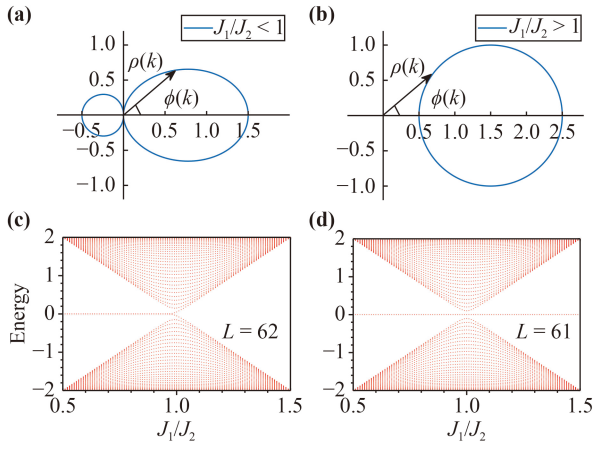

Fig. 2 Two types of trajectories of the vector $\boldsymbol{g}(k)$ with different topologies when k runs across the Brillouin zone: **(a)** $J_1/J_2 < 1$ and **(b)** $J_1/J_2 > 1$. The spectrum of the SSH model versus J_1/J_2 for the even size $L = 2N = 62$ of chain in **(c)** and the odd size $L = 2N - 1 = 61$ in **(d)**.

In this protocol, the size of superconducting qutrit-resonator chain is restricted to the odd number, the interaction Hamiltonian of which can be written as $H_{2N-1} = \sum_{n=1}^{N-1} J_1 b_n S_n^{\dagger} + J_2 b_n S_{n+1}^{\dagger} + \mathrm{H.c.}$. Accordingly, the topological protected zero-mode edge state of the odd-sized chain with a single excitation are exponentially localized at the boundaries, which can be obtained analytically (see Appendix A for details)

$$|\varphi_E\rangle = \sum_{n=1}^{N} \lambda^n \sigma_n^{+}(\sigma_n^x)^{n-1} \bigotimes_{l=1}^{n-1} \sigma_l^x |G\rangle_L, \tag{9}$$

where $\sigma_n^{+} = |e\rangle_n\langle R|$ and $|G\rangle_L = |RLR\cdots\rangle_{A_N} \otimes |000\cdots\rangle_{B_{N-1}}$ denotes a decoupled state of the qutrit-resonator chain with A_1 in $|R\rangle$, B_1 in $|0\rangle$ (zero-photon Fock state), A_2 in $|L\rangle$, B_2 in $|0\rangle$, ... and $\lambda = -J_1/J_2$. The system can perform a topologically protected state transfer on the zero mode from the left edge to the right edge, corresponding to an excitation transfer from one side to the other, when setting initially $J_1/J_2 = 0$ while finally $J_1/J_2 = +\infty$.

It is evident that the above topological protected transfer process needs to satisfy the adiabatic limit [8, 12, 13]. A sufficient condition for the adiabatic evolution is $\Delta E = |E_m(t) - E_n(t)| \gg |\langle\dot{\varphi}_m(t)|\varphi_n(t)\rangle|$, where E_m, E_n, $|\varphi_m(t)\rangle$ and $|\varphi_n(t)\rangle$ are the mth and nth instantaneous eigenenergies and corresponding eigenstates of the Hamiltonian, and the overdot indicates differentiation with respect to time. In general, the eigenenergy difference $|E_m(t) - E_n(t)|$ between $|\varphi_m(t)\rangle$ and $|\varphi_n(t)\rangle$ is very small. Therefore, for the sake of satisfying the adiabatic limit, the time evolution of the adiabatic state transfer should be very slow to make the evolution remain in the zero mode (edge state) without exciting other eigenstates (bulk states) due to a trivial ΔE. The adiabatic limit condition can be relaxed to realize fast topological pumping by increasing the eigenenergy difference ΔE to form a nontrivial band gap in the Hamiltonian spectrum or/and decreasing the derivative of the Hamiltonian.

In order to realize fast topological pumping of edge states by relaxing the adiabatic limit condition, it is crucial to suitably adjust the coupling strengths. Here we specify that the couplings are shaped by an exponential function

$$J_1 = J_0\left(\frac{1-\mathrm{e}^{-\alpha t/T}}{1-\mathrm{e}^{-\alpha}}\right),$$
$$J_2 = J_0\left[\frac{1-\mathrm{e}^{-\alpha(T-t)/T}}{1-\mathrm{e}^{-\alpha}}\right], \tag{10}$$

where T is the total evolution time and α a free parameter that can be fine-tuned [12]. The forms of $J_{1,2}$ in Eq. (10) satisfy the state transfer conditions $J_1/J_2|_{t\to 0} = 0$ and $J_1/J_2|_{t\to T} = +\infty$ well. To illustrate the crucial characteristics of topological pumping for coupling strengths and analyze how the energy spectrum evolves over time, the functions of coupling strengths and the corresponding instantaneous energy spectrum versus time are plotted in the left plane and the right plane of Fig. 3, respectively. We take the size $L = 2N-1 = 61$ of the chain as an example and select three different values of free parameter $\alpha = 1$ in (a) and (b), $\alpha = 6$ in (c) and (d), and $\alpha = 11$ in (e) and (f), respectively. In the odd-sized chain, there is always one zero-mode state remaining unchanged and is separated from bulk states, shown in the right plane of Fig. 3. At the beginning, the energy gap separating the edge state from the bulk states takes its maximum value. Subsequently, the energy gap approaches its minimum, occurring at $J_1 = J_2$, and at the end of evolution time the energy gap regains its maximum value.

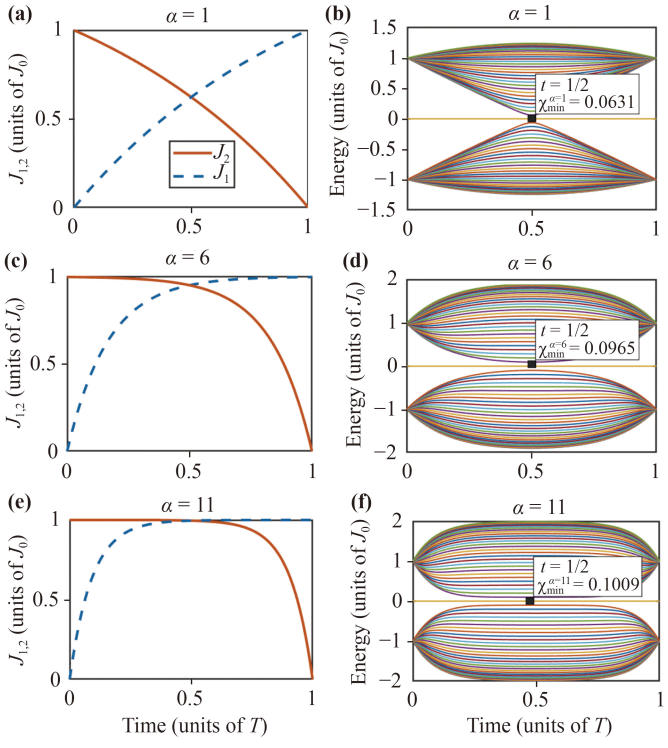

Fig. 3 Functions $J_{1,2}$ and the corresponding instantaneous energy spectrum as a function of time by setting different parameters $\alpha = 1$ in **(a)** and **(b)**, $\alpha = 6$ in **(c)** and **(d)**, and $\alpha = 11$ in **(e)** and **(f)**. We choose the total evolution time to be unity and the size of chain is $L = 2N-1 = 61$.

Comparing the functions with different values of free parameter α employed in the topological chain, we can notice their qualitative differences. In particular, there is the most significant eigenenergy difference ΔE between the bulk state and the edge state for the smallest value of α. The functions with $\alpha = 1$ approach the minimum value of the energy gap with the largest slope, while the functions with $\alpha = 11$ drive the system more gently in this region, shown in the left planes of Fig. 3. Depending on the value of free parameter α, the minimum value of energy gap can be changed, which is the key point to avoid nonadiabatic effects and to speed the state transfer. For the odd-sized chain with length L, the eigenmode energies (besides the zero-energy solution) can be analytically given by

$$g = |J_1 + J_2\mathrm{e}^{\mathrm{i}q_m}|, \tag{11}$$

where $q_m = 2m\pi/(L+1)$ with $m = 1, 2, \cdots, [L/2]$, and we define that $[z]$ gives the greatest integer that is less than equal to z [94]. Thus, the energy gap can be analytically determined by $\chi = 2|g_{[L/2]}|$, which is related to the values of J_1 and J_2. Note here that, there always exists a time such that $J_1 = J_2$. In the fast topological pumping with exponential couplings, we consider this time to be $t = T/2$ in the right plane of Fig. 3. In the infinite system, $J_1 = J_2$ corresponds to the closing of the energy gap separating the zero-mode state with the rest of energy states. Thus, the point in the parameter space where the coupling strengths J_1 and J_2 are equal corresponds to the minimum value of energy gap $\chi_{\min}$ during the whole evolution process. The minimum values of energy gap are analytically obtained by $\chi_{\min}^{\alpha=1} = 0.0631J_0$, $\chi_{\min}^{\alpha=6} = 0.0965J_0$ and $\chi_{\min}^{\alpha=11} = 0.1009J_0$, which are labeled with tags in the right plane of Fig. 3.

Based on time-dependent exponential couplings with different values of the free parameter α, we plot the state distribution of the zero mode versus evolution time in Figs. 4(a)–(c). The population of zero-mode state is defined by $P(t) = \langle\varphi_E|\rho(t)|\varphi_E\rangle$, where $|\varphi_E\rangle$ and $\rho(t)$ are the target zero-mode state and the time-dependent density matrix of the system by solving Liouville equation $\dot{\rho}(t) = -\mathrm{i}[H_{2N-1}, \rho(t)]$, and t corresponds to the evolution instant. Concretely, the dark blue fringes show that almost no population of zero-mode state is distributed in the lattice sites. However, the bright yellow fringes indicate that population about 0.2 of zero-mode state is emerged in the even lattice sites at the specific evolution moments. The most bright yellow fringes mean that near-unity population of zero-mode state appears in the first and the last lattice sites at the begin and end of evolution. In Figs. 4(a)–(c), the zero-mode state is localized at the first site A_1 or the last A_{61} and the distribution of left or right edge state with zero mode is equal to unity when $J_0 t \to 0$ or $J_0 t \to +\infty$ to realize the topological protected edge state transfer in the odd-sized SSH chain.

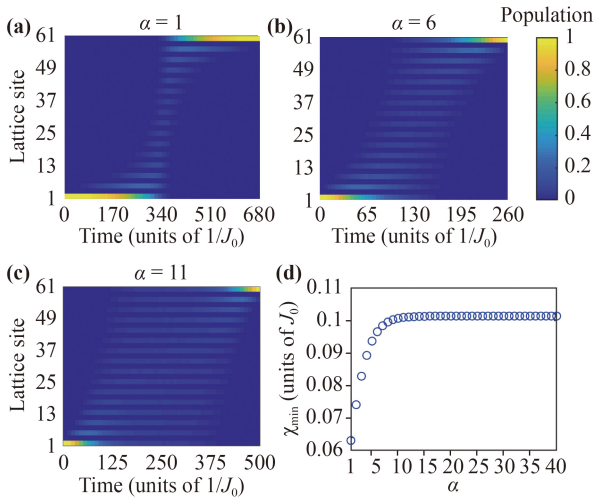

Fig. 4 The evolution process of zero-energy mode with different values of the parameters $\alpha = 1$ in **(a)**, $\alpha = 6$ in **(b)** and $\alpha = 11$ in **(c)**. **(d)** Numerical scatters of the minimum energy gap versus values of α with the size of chain $L = 2N - 1 = 61$.

To be specific, the value of parameter α is related to the total evolution time. It is noted that the shortest evolution time with the size of chain $L = 2N - 1 = 61$ approaches to $T = 260/J_0$ under the condition of $\alpha = 6$. Besides, the distribution of zero-mode state at odd sites are enlarged by increasing the value of parameter α in the time scale, seen from bright fringes in Figs. 4(a)–(c). However, the population of zero mode increases exponentially on the odd sites (qutrits) while the zero-mode state exhibits no populations on the even sites (resonators), indicating the virtual photon excitation in the resonators. The reason lies in the interaction property of the system, that is, the formulation of the Hamiltonian, which determines that the distribution of zero-mode state of system on different lattice sites. In the SSH model, according to $H_{2N-1}|\varphi_E\rangle = 0$, one can calculate the analytic form of the zero-mode state of the system (see Appendix A), for which it is exactly one of the most important features of the SSH model that the zero-mode state only distributes on odd-size lattice sites while involves no even-size ones.

As shown in Fig. 4(d), by selecting different α and the corresponding minimum energy gap as numerical samples, it can be found that the maximization of minimum energy gap needs a large value of parameter α. A larger value of parameter α ($\alpha \in [1, 11]$) determines J_1 and J_2 to equate at a higher value. As for $\alpha \geq 11$, the minimum energy gap can be maximized and keeps around $0.1J_0$ because equating J_1 and J_2 at values close to the maximum value of couplings can be acquired during the transfer. On the one hand, the minimum energy gap can be actually used to specify a characteristic timescale. It can be assumed that the system is close to the adiabatic following of the zero-mode state, under the condition of the sufficiently longer transfer time by comparing with this timescale. On the other hand, the coupling functions are required with the steeper slope at first and the smaller slope at the middle time of evolution. In view of the above two key characteristics of the coupling functions, the exponential function with the tunable parameter α seems to be one of the most appropriate to increase the speed of the transfer protocol.

3 Fast generation of large-scale GHZ states with great robustness and scalability

3.1 Fast generation of large-scale GHZ states

We focus on the generation of large-scale GHZ states among the N qutrits based on the fast topological pumping via edge states. The implementation of zero-mode edge state transfer by engineering exponential coupling functions via the topological protected edge channel has been shown in Figs. 4(a)–(c). Thus, the left and right edge states localized in the odd-sized chain at the beginning and end of evolution time can be expressed, respectively, as

$$\begin{aligned} |l\rangle_L &= |eLR\cdots m\rangle_{A_N} \otimes |000\cdots 0\rangle_{B_{N-1}}, \\ |r\rangle_L &= |LRL\cdots e\rangle_{A_N} \otimes |000\cdots 0\rangle_{B_{N-1}}, \end{aligned} \tag{12}$$

where $m = R\,(L)$ when N is odd (even). Initially, we suppose that the state of the chain is $|\Psi_0\rangle = (|G\rangle_L + |l\rangle_L)/\sqrt{2}$ meaning that the first qutrit are prepared in a superpostion $(|R\rangle + |e\rangle)/\sqrt{2}$. The evolution via the protected edge channel takes the form of

$$\begin{aligned} |G\rangle_L &\longrightarrow |G\rangle_L, \\ |l\rangle_L &\longrightarrow -(-1)^N |r\rangle_L, \end{aligned} \tag{13}$$

which is irrelevant with the state $|G\rangle_L$ because of zero-photon in the resonators that cannot excite the ground-state qutrits. We specify that logical states 0 and 1 are carried by the ground levels $|L\rangle$ and $|R\rangle$, respectively, for the qutrit A_n $(1 \leq n \leq N-1)$. As for the last qutrit A_N, we set that $|e\rangle$ is employed by the logical state 1 (0) when N is even (odd). Consequently, a large-scale GHZ state of N qutrits without regard to the zero-photon product state of resonators is obtained and reads as

$$\frac{1}{\sqrt{2}}(|101\cdots 1(0)\rangle_{A_N} - (-1)^N |010\cdots 0(1)\rangle_{A_N}). \tag{14}$$

This is exactly an N-body GHZ state according to a general form of x-qubit GHZ state which can be expressed as $(|m_1 m_2 m_3 \cdots m_x\rangle + \mathrm{e}^{\mathrm{i}\phi}|n_1 n_2 n_3 \cdots n_x\rangle)/\sqrt{2}$ where $m_j + n_j = 1$ $(m_j, n_j \in 0, 1)$ [95–98].

In the following, we take $\alpha = 6$ as an example and consider $L = 61$ to plot the evolution of population based on the fast topological pumping with exponential

couplings and the conventional adiabatic topological pumping with Gauss couplings [15] for the ideal 31-body GHZ state $|\Psi_{\text{ideal}}\rangle = (|G\rangle_{61} + |r\rangle_{61})/\sqrt{2}$, the initial state $|\Psi_{\text{initial}}\rangle = (|G\rangle_{61} + |l\rangle_{61})/\sqrt{2}$, the left edge state $|l\rangle_{61} = |eLR\cdots R\rangle_{A_{31}} \otimes |000\cdots 0\rangle_{B_{30}}$, the right edge state $|r\rangle_{61} = |LRL\cdots e\rangle_{A_{31}} \otimes |000\cdots 0\rangle_{B_{30}}$ and the decoupled state $|G\rangle_{61} = |RLR\cdots\rangle_{A_{31}} \otimes |000\cdots 0\rangle_{B_{30}}$. As expected in Fig. 5(a), a complete state transfer from the left edge state $|l\rangle_{61}$ to the right edge state $|r\rangle_{61}$ is manifested and the decoupled state $|G\rangle_{61}$ remains unchanged, resulting in the successful creation of a 31-body GHZ state in both fast topological pumping with exponential couplings and the conventional adiabatic topological pumping with Gauss couplings. However, the populations of states $|r\rangle_{61}$, $|l\rangle_{61}$, $|\Psi_{\text{initial}}\rangle$ and $|\Psi_{\text{ideal}}\rangle$ based on the fast topological pumping with exponential couplings tends to 0.5, 0, 0.25 and 0.999, respectively, only at the end of evolution time. In respect to the conventional adiabatic topological pumping, the population of those states can also attain relatively ideal results at $t \approx 5000/J_0$ and keep unchanged until at the end of evolution time.

In order to verify the generation of the large-scale GHZ state via fast topological pumping in a short evolution time, we make a comparison between this protocol and the conventional adiabatic topological pumping. The quantity that determines how faithfully the evolution has occurred is the fidelity, which can be formulated as $F(t) = \langle\Psi_{\text{ideal}}|\rho(t)|\Psi_{\text{ideal}}\rangle$, where $|\Psi_{\text{ideal}}\rangle$ and $\rho(t)$ are the target state and the time-dependent density matrix of the system by solving Liouville equation $\dot{\rho}(t) = -\mathrm{i}[H_{2N-1}, \rho]$, and t corresponds to the evolution instant. In Fig. 5(b), for each protocol, we plot the final fidelity $F(T)$ as a function of the total evolution time T. In the case of reaching the fidelity of 0.999, it can be found that the protocol with exponential couplings based on the fast topological pumping is greatly faster than that with Gaussian couplings, because of the former occurring at $T_{\text{Exp}} \approx 390/J_0$ as compared to the latter where this happens at $T_{\text{Gauss}} \approx 4293/J_0$. Figure 5 indicates the successful and fast creation of large-scale GHZ state via the fast topological pumping in this protocol.

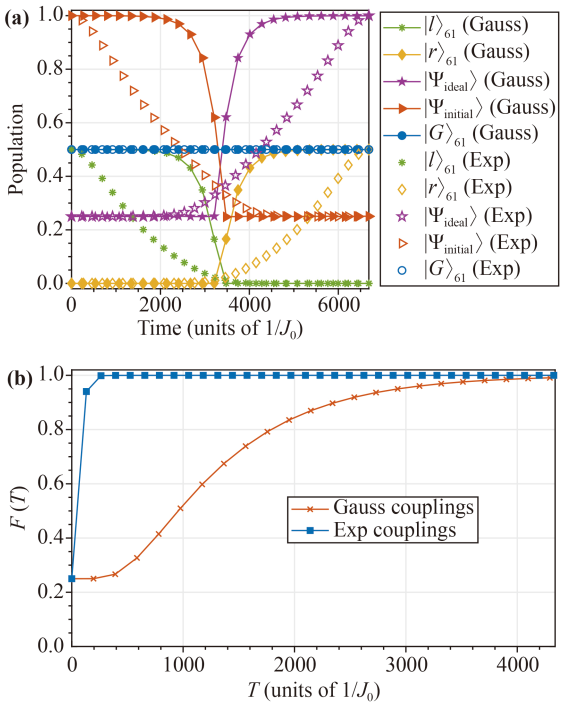

Fig. 5 **(a)** Population evolution of states $|r\rangle_{61}$, $|l\rangle_{61}$, $|G\rangle_{61}$, $|\Psi_{\text{ideal}}\rangle$ and $|\Psi_{\text{initial}}\rangle$ based on fast topological pumping with exponential couplings and the conventional adiabatic topological pumping with Gauss couplings. **(b)** Final fidelity of 31-body GHZ state $|\Psi_{\text{ideal}}\rangle$ as a function of the total evolution time T based on fast topological pumping with exponential couplings and the conventional adiabatic topological pumping with Gauss couplings. We choose the size of chain as $L = 2N - 1 = 61$ and set the free parameter $\alpha = 6$.

3.2 Effect of different values of α

The implementation of fast topological pumping via edge channels for generating large-scale GHZ states in an odd-sized topological chain has been shown above, which takes the free parameter $\alpha = 6$ as an example. Now that the qualitative differences among coupling functions, energy spectrum and the distribution of the zero-energy mode for different values of free parameter α have become apparent in 2.2 here we further examine some quantitative results for generating large-scale GHZ states based on the fast topological pumping.

In the following, Figs. 6(a)–(c) show that the final fidelities of 5, 18 and 31-body GHZ state as functions of the total evolution time by setting $\alpha = 1, 6, 11, 16$ and 21, respectively. Apparently, an N-body GHZ state needs a longer total evolution time with the increase of N. In the limit of $T \to +\infty$, the fidelity of N-body GHZ state approaches unity for all the α parameters, which indicates a perfect transfer of excitation along the chain. In Fig. 6(a), there are slight differences among different values of α for the total evolution time of 5-body GHZ state. However, it can be noticed that the fidelity curve tends to oscillate for $TJ_0 \in [20, 100]$, owing to the action of resonant processes. As for the 18- and 31-body GHZ states in Figs. 6(b) and (c), there are more significant oscillations for $\alpha = 11, 16$ and 21, respectively.

According to the adiabatic condition, the oscillations during the evolution are strongly associated with the energy gap between the zero-mode energy E_N and the most-closed-to-zero eigenenergy E_{N+1}. In order to study the oscillations appearing in the fidelity of 5-, 18- and 31-body GHZ states, the corresponding instantaneous energy E_{N+1} in cases of $\alpha = 1, 6, 11, 16$ and 21 are plotted in the bottom plane of Fig. 6. As for the small-scale GHZ state of $N = 5$ in Fig. 6(d), the parameter values $\alpha = 6, 11, 16$ and 21 have almost same effects on the corresponding instantaneous energy E_{N+1}. When

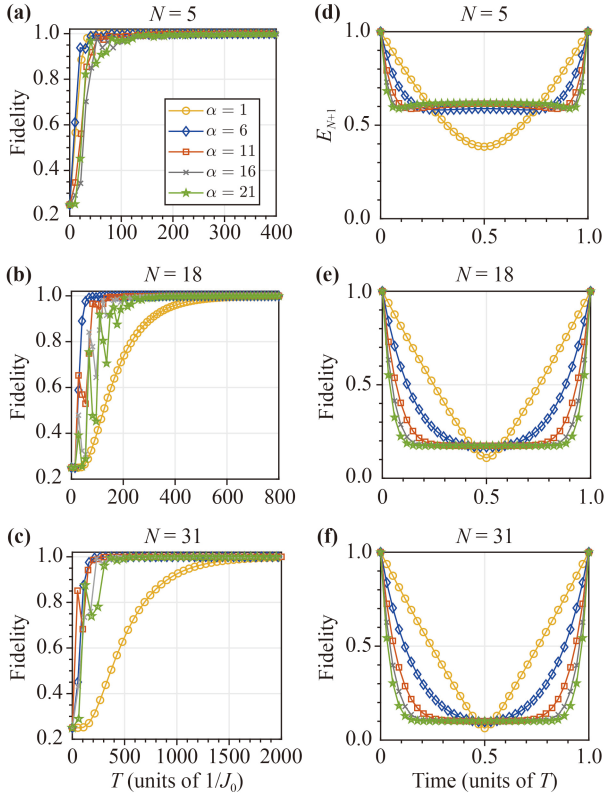

Fig. 6 **(a–c)** Final fidelity of N-body GHZ state as a function of the total evolution time with different values of the parameter α by increasing the number of qutrits $N = 5$ in **(a)**, $N = 18$ in **(b)** and $N = 31$ in **(c)**. **(d–f)** The corresponding instantaneous energy E_{N+1} as a function of time with different values of the parameter α by increasing the number of qutrits $N = 5$ in **(d)**, $N = 18$ in **(e)** and $N = 31$ in **(f)**.

$t \in [0.1, 0.9]T$, the instantaneous energy $E_{N+1} \approx 0.6J_0$ is always closed to the zero-mode energy so that the slight oscillations appear in the adiabatic evolution process. However, the instantaneous energy $E_{N+1} \approx 0.4J_0$ in the case of the parameter $\alpha = 1$ approaches to zero-mode energy only at the middle of evolution, closer to zero so that the resonance process is inhibited inconspicuously when compared with cases of other α. In Fig. 6(e) for generating 18-body GHZ state, the instantaneous energy E_{N+1} indicates similar evolution in cases of $\alpha = 11, 16$ and 21 to form the most obvious oscillations in Fig. 6(b). In respect to the cases of the parameter $\alpha = 1$ and 6, there is few oscillations during the adiabatic evolution owing to the greater and greater separation between the zero-mode energy and the energy E_{N+1} except for the middle of evolution in Fig. 6(e). By increasing N in Fig. 6(f), the corresponding instantaneous energy E_{N+1} of 31-body GHZ state with different values of α verges on the zero-mode energy more closely in contrast to 5- and 18-body GHZ state. When concentrating on the total evolution time T for different values of α, the decreasing value of energy gap between the zero-mode energy and the energy E_{N+1} indicates longer evolution time to attain high fidelity N-body GHZ states. Nevertheless, the resonant processes can be properly handled to generate the large-scale GHZ state with a high efficiency by tuning the parameter α.

Actually, the above phenomenon can be further understood by characteristics of coupling functions and the corresponding energy spectrum in Fig. 3. Smaller values of the parameter α lead to a less steep slope of the coupling function, resulting J_1 and J_2 equating at a smaller value. Simultaneously, the topological edge state at zero energy is separated from bulk states better as the function of evolution time except for $t = T/2$. Owing to a better separation between the edge state and the bulk states, the resonant processes can be suppressed effectively. Specially, the minimum value of energy gap $\chi_{\min}$ is demanded as large as possible, which makes the chain evolve adiabatically along the zero-mode edge state without exciting other eigenstates at $t = T/2$. Therefore, the parameter α is closely related to two aspects, a smaller value for suppressing the nonadiabatic transition between the edge state and bulk states and a larger value for obtaining a greater $\chi_{\min}$. Typically, a suitable value of parameter α is the key point to generate high fidelity of N-body GHZ state based on the fast topological pumping, which can not only avoid the resonant processes but also shorten the total evolution time.

In the following, we investigate the fidelity of 5-, 18-, 31- and 44-body GHZ states versus the varying α and the total evolution time T in Figs. 7(a)–(d), respectively. In Fig. 7(a), the appropriate range of the parameter α is chosen as $\alpha \in [1, 6]$ to generate 5-body GHZ state with the high fidelity and the short total evolution time. The 0.995 and 0.999 fidelity contour lines exhibit strongly oscillations for all values of the parameter α and the total evolution time T, which is similar to Fig. 6(a). As

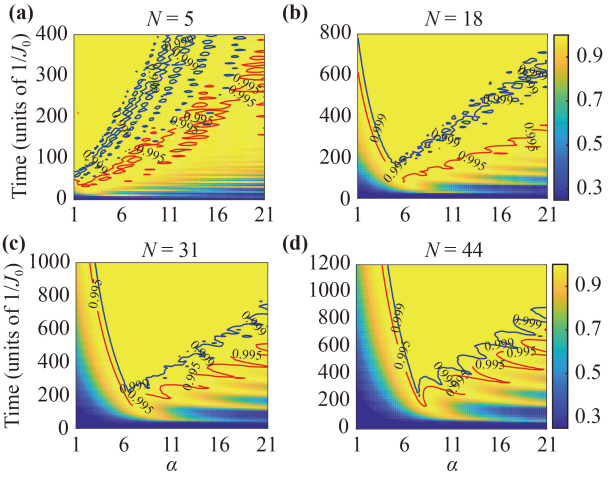

Fig. 7 The fidelity of N-body GHZ state versus the varying α and the total evolution time T for **(a)** $N = 5$, **(b)** $N = 18$, **(c)** $N = 31$ and **(d)** $N = 44$. The red and blue solid lines represent 0.995 and 0.999 fidelity contour lines of N-body GHZ state, respectively.

for 18- and 31-body GHZ states in Figs. 7(c) and (d), respectively, N-body GHZ state with the high fidelity and the short total evolution time demands the parameter $\alpha \in [6, 11]$ approximately. Considering the 0.995 and 0.999 fidelity contour lines of 18-, 31- and 44-body GHZ states, the oscillations are suppressed substantially under the range of $\alpha \in [1, 6]$. Based on the fast topological pumping for generation of N-body GHZ state, it is no wonder that the value of parameter $\alpha = 6$ is a trade-off, since the chain is driven strongly to increase the speed but also gently enough to avoid resonant processes.

In order to more intuitively reflect the speed of protocols for the fast topological pumping and the conventional adabatic topological pumping, we select different N and corresponding evolution times of generating GHZ states with the fidelity of 99.9% as numerical samples to fit the function of the total evolution time T versus N in Fig. 8(a). The fitting functions for Gauss and exponential couplings are $J_0T = 6.9419N^2 + 2.455N - 59.8933$ and $J_0T = 0.3691N^2 - 2.06N + 25.9$, respectively. As N increases, the total evolution time of GHZ state shows a quadratic trend with N for both the Gauss and exponential couplings. However, an 80-body GHZ state with 99.9% fidelity requires the total evolution time $T_{\text{Exp}} \approx 35.4$ μs but $T_{\text{Gauss}} \approx 711$ μs by choosing the value of $J_0 = 2\pi \times 10$ MHz [99]. In order to get the information from the shortest time of generating N-body GHZ states in the small scale based on the fast topological pumping with exponential couplings and the conventional adiabatic pumping with Gauss couplings, we numerically calculate the fidelity of ideal N-body GHZ states in the small scale, and plot the time evolution of $\log_{10}(1 - F)$ with N ranging from 10 to 30 at intervals of 5 in Fig. 8(b). The numerical results based on the conventional adiabatic pumping exhibit that a higher fidelity needs a longer evolution time with increasing N. As for the fast topological pumping, the evolution time for attaining 0.999 fidelity of N-body GHZ state has a trivial difference among different values of N in contrast to the conventional adiabatic pumping when $10 < N < 30$ by enlarging the range of $T \in [0, 300]/J_0$, owing to the instantaneous energy spectrum characteristics of small-scale systems based on the fast topological pumping. It is evident that the efficiency of evolution based on the fast topological pumping improves more significantly with a larger N than the conventional topological pumping.

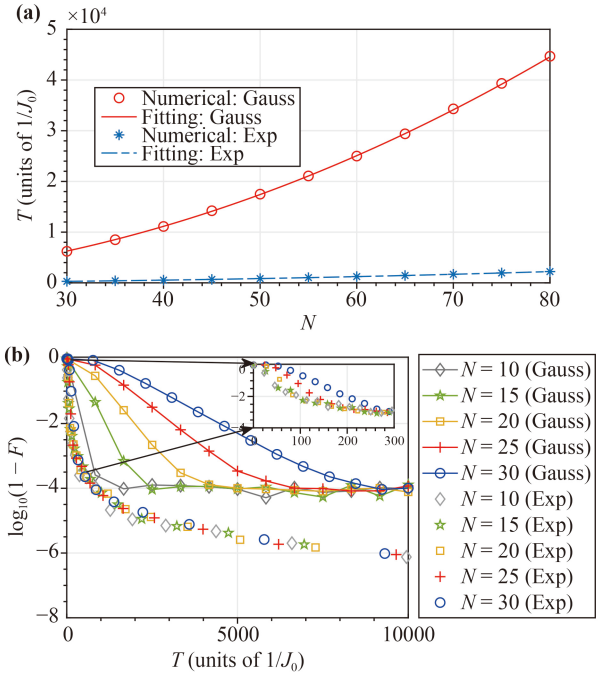

Fig. 8 **(a)** Fitting functions and numerical scatters between the number of qutrits and total evolution time with 99.9% fidelity for the conventional adiabatic topological pumping with Gauss couplings and the fast topological pumping with exponential couplings. **(b)** Time evolution of $\log_{10}(1 - F)$ for generating N-body GHZ states with N ranging from 10 to 30 at intervals of 5 based on the conventional adiabatic pumping with Gauss couplings and the fast topological pumping with exponential couplings, respectively.

3.3 Robustness against disorders and losses in the superconducting qutrit-resonator chain

The one-dimensional superconducting qutrit-resonator chain may possess not only itself defects and perturbation but also dissipative processes, which could result in infidelities for the perfect generation of N-body GHZ states. Three dominant aspects of influence are considered here: (i) unwanted on-site potential defects for qutrits A_n and resonators B_n; (ii) inevitable variation in ideal couplings; (iii) losses of qutrits A_n and resonators B_n with decay rates κ_n and γ_n, respectively.

In order to study the robustness of the protocol against the on-site potential defects and the variation of ideal couplings, the chain can be described by

$$H_d = \sum_{n=1}^{N} \delta_{A,n} |e\rangle_n\langle e| + \sum_{n=1}^{N-1} \delta_{B,n} b_n^\dagger b_n + \sum_{n=1}^{N-1} \left(J'_{1,n} |e\rangle_n\langle j_n| + J'_{2,n} |e\rangle_{n+1}\langle j_n| \right) b_n + \text{H.c.}, \tag{15}$$

where $J'_{1(2),n} = J_{1(2)} + \text{rand}[-\delta_{J_{1,2}}, \delta_{J_{1,2}}]$, $\delta_{A(B),n} = \text{rand}[-\delta_{A(B),n}, \delta_{A(B),n}]$ and $\text{rand}[-x, x]$ denotes a random number in the range of $[-x, x]$. For convenience, the disorder strengths of on-site potential defects and couplings are chosen as $\delta_{A(B),n} = \delta_{J_{1,2},n} = \delta$ as an example. The relation between the fidelity of 31-body GHZ state and the disorder $\delta \in [0, 0.5]$ is exhibited in Fig. 9. It is the disorder that is randomly sampled among 10 000 times, and then the fidelity is taken as an average of the 10 000 results versus the disorder of potential defects for all A-type lattice sites, B-type lattice sites and coupling strengths, respectively. The fidelity shows relatively great robustness

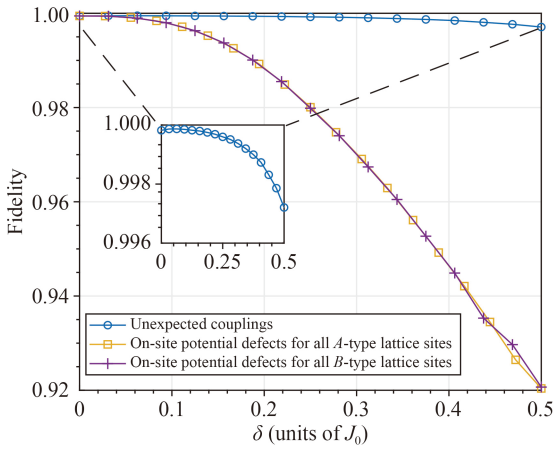

Fig. 9 Final fidelity of 31-body GHZ state against the unexpected coupling strength and the on-site potential defect for all A-type lattice sites and B-type lattice sites with disorder δ.

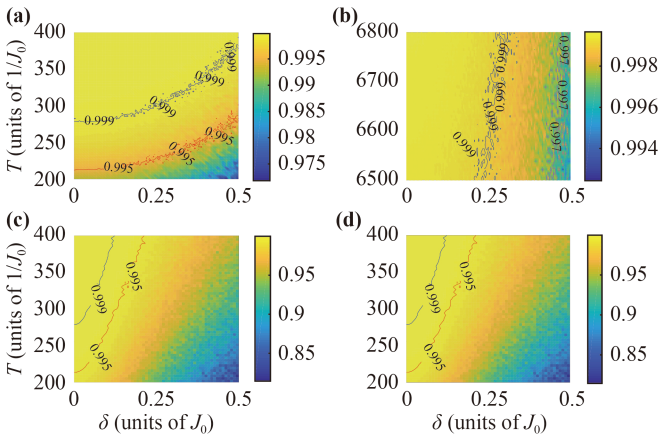

Fig. 10 The fidelity of the 31-body GHZ state versus the varying δ and the total evolution time T for unexpected couplings with exponential couplings in **(a)** and with Gauss couplings in **(b)** and for on-site potential defect with A-type lattice sites in **(c)** and with B-type lattice sites in **(d)**. The red (purple) and blue solid lines represent 0.995 (0.997) and 0.999 fidelity contour lines of N-body GHZ state, respectively.

for the disorder of coupling strengths and on-site potential defects. By magnifying the disorder for coupling strengths, the fidelity of 31-body GHZ state keeps still above 99.6%. The yellow-squared and purple-crossed lines indicate that the on-site potential defects for all B-type lattice sites and all A-type lattice sites cause the same degree damage to the fidelity of 31-body GHZ state, which can retain 91% even if $\delta = 0.5$. The robustness of N-body GHZ state to the disturbance and perturbation benefits not only from the topological protected edge channel but also the improvement of evolutionary efficiency, which will show a more obvious superiority even when increasing N.

Furthermore, we also investigate the relation among the fidelity of 31-body GHZ state, the total evolution time T and the disorder δ for unexpected couplings, on-site potential defects of A- and B-type lattice sites based on the fast topological pumping in Figs. 10(a), (c) and (d), respectively. The damage to fidelity caused by unexpected couplings and on-site potential defects for all A- and B-type lattice sites with $\delta/J_0 \in [0.2, 0.5]$ can be compensated by longer evolution time T. Specially, we show 0.995 and 0.999 fidelity contour lines of 31-body GHZ state in Figs. 10(a), (c) and (d), respectively. The robustness against the disorder from unexpected couplings shows a greater result than that from on-site potential defects due to the topological property, which is equivalent to Fig. 9. Also, the relation among the fidelity of 31-body GHZ state, the total evolution time T and the disorder δ for unexpected couplings based on the conventional adiabatic topological pumping is exhibited in Fig. 10(b). The conventional adiabatic topological pumping shows the more robustness against the unexpected couplings than the fast topological pumping, learning from the red contour lines in Figs. 10(a) and (b). This result comes from the fact that the conventional adiabatic topological pumping needs a longer adiabatic evolution time to offset the damage on the fidelity from the unexpected couplings than the fast topological pumping, indicating that the improvement in speed based on the fast topological pumping is in cost of robustness against disorder from the unexpected couplings.

The robustness against disorders is benefit from the topological property of the system, which can trace back to the chiral symmetry in the system. Concretely, the system is satisfied with $\Gamma H_{2N-1}\Gamma^{-1} = -H_{2N-1}$, where $\Gamma = \prod_n (S_n^\dagger S_n - b_n^\dagger b_n) = \prod_n \sigma_z$ [93, 100]. Meanwhile, this symmetry indicates that the zero-energy mode can exist and results in a symmetric energy spectrum with each positive eigenenergy E accompanied by a negative eigenenergy $-E$. From an algebraic point of view, the Bloch Hamiltonian of the chain $\mathcal{H}^B$ in Eq. (4) can be written as a linear combination of the Pauli matrices σ_x and σ_y while is irrelevant to σ_z. Thus, in the presence of unexpected couplings $J'_{1,2}$, the system still obeys the chiral symmetry. Besides, the robustness against the disorder from the unexpected couplings also profits from adiabatic passage of generating large-scale GHZ state based on fast topological pumping. The reason lies in that the exponential couplings are related to the adiabatic evolution time while on-site potential defects for all A- and B-type lattice sites are constant terms. However, the presence of on-site potential defects breaks the chiral symmetry of this system and modifies the energies of the edge state. For a large disorder, these states cannot be distinguished from the bulk. Consequently, the evolution along the zero-mode edge state may be affected gently from the on-site potential defects for qutrits and resonators while hardly from the unexpected couplings.

We now take the effects of losses of qutrits and resonators on the fidelity of GHZ states based on the

fast topological pumping. The dynamics of the lossy system affected by the two dominant channels for the losses of qutrits and resonators, respectively, can be governed by the non-Hermitian Liouville equation $\dot{\rho} = -\mathrm{i}(H^{'}\rho - \rho H^{'\dagger})$, where $H^{'} = H_{2N-1} - \mathrm{i}\kappa_n \sum_{n=1}^{N-1} b_n^{\dagger} b_n / 2 - \mathrm{i}\gamma_n \sum_{n=1}^{N} |e\rangle_n\langle e|/2$ [58, 101]. For convenience, we assume that $\kappa_n = \kappa$, $\gamma_{q_n} = \gamma_q$ and $J_0/(2\pi) = 10$ MHz. Figure 11 shows the final fidelity versus the resonator decay rate κ and the qutrit decay rate γ_q based on the conventional adiabatic topological pumping with Gauss couplings and the fast topological pumping with exponential couplings. The upper and lower surfaces indicate that the qutrit decay brings down the fidelity significantly as γ_q increases, while the loss of resonators has slight effect on the fidelity, owing to the virtual excitation of photon in the resonator B_n. As for the fast protocol with exponential couplings, the fidelity is improved apparently in contrast to the lower surface for the conventional adiabatic topological pumping with Gauss couplings. When $\kappa/(2\pi) = \gamma_q/(2\pi) = 3$ kHz [102, 103], the fidelity of 31-body GHZ state can reach around 25% and 65.25% for Gauss and exponential couplings, respectively. The above results manifest the protocol based on the fast topological pumping enhances robustness largely against losses of the resonators and qutrits.

3.4 Scalability of GHZ states

As stated above, our protocol shows a remarkable improvement against both disorders and losses in the chain. This robustness is not only related to topological protection, as well as the enhancement of evolutionary efficiency, which stems from the short timescales to enable the fast topological pumping according to the crucial characteristics of energy spectrum and zero-mode edge state transfer.

In order to verify more quantitatively the effect of our protocol, one more vital direction is the scalability of GHZ state. In the following, we take into account the losses of qutrits and resonators with different coupling strengths $J_0/(2\pi) = 1, 10$ and 50 MHz. For the fixed and experimentally available decay rates of qutrits and resonators with $\gamma_q/(2\pi) = \kappa/(2\pi) = 1$ kHz [104–108], the relation between final fidelities of GHZ states and the scalability of entanglement N are exhibited in Fig. 12. The unmarked and marked lines represent the conventional adaibatic topological pumping with Gauss couplings and the fast topological pumping with exponential couplings, respectively. Obviously, the fidelity exhibits decreasing tendency with increasing N for both two protocols. However, a greater value of coupling strength J_0 can be applied to effectively suppress the trend of decline. Furthermore, the advantage of our protocol becomes more pronounced as the scalability of GHZ state is strengthened for the fast topological pumping with exponential couplings. When $J_0/(2\pi) = 1$ MHz, the fidelity of 30-body GHZ state can stay above 90% for exponential couplings while just 35% for Gauss couplings. As for the GHZ state with $N = 150$ and the coupling strength $J_0/(2\pi) = 50$ MHz, the fidelity of the fast topological pumping and the conventional topological pumping can reach 88% and 50%, respectively. Thus, by inspecting Fig. 12, it is evident that the fast topological pumping outperforms a lot the conventional adaibatic topological pumping in terms of the scalability of entanglement N.

Furthermore, we consider the scalability of N-body GHZ state in a two-dimensional square lattice with the size of $L \times L$ based on the superconducting qutrit-resonator system in Fig. 13. The fast topological pumping occurs at the ith line and the $(2N-1)$th column of SSH chain to generate N-body GHZ states, including three

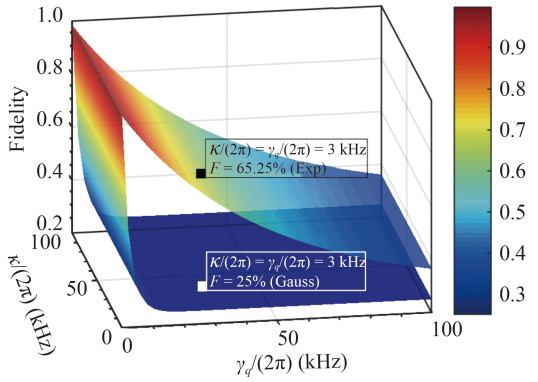

Fig. 11 Effects of losses on the final fidelity of 31-body GHZ state for the conventional adiabatic topological pumping with Gauss couplings and the fast pumping with exponential couplings. We choose $J_0/(2\pi) = 10$ MHz, the corresponding total evolution time $T_{\mathrm{Gauss}}^{N=31} = 106.42$ μs and $T_{\mathrm{Exp}}^{N=31} = 5.04$ μs with a 99.9% fidelity for generating a 31-body GHZ state.

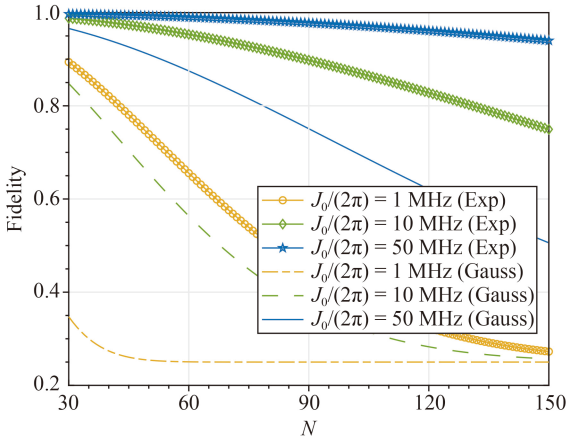

Fig. 12 Final fidelities of the GHZ state with the scalability of entanglement N under the coupling strengths (e.g., $J_0/(2\pi) = 1$ MHz, 10 MHz and 50 MHz) and decay rates of qutrits and resonators (e.g., $\gamma_q/(2\pi) = \kappa/(2\pi) = 1$ kHz) for the conventional adiabatic topological pumping with Gauss couplings and the fast topological pumping with exponential couplings.

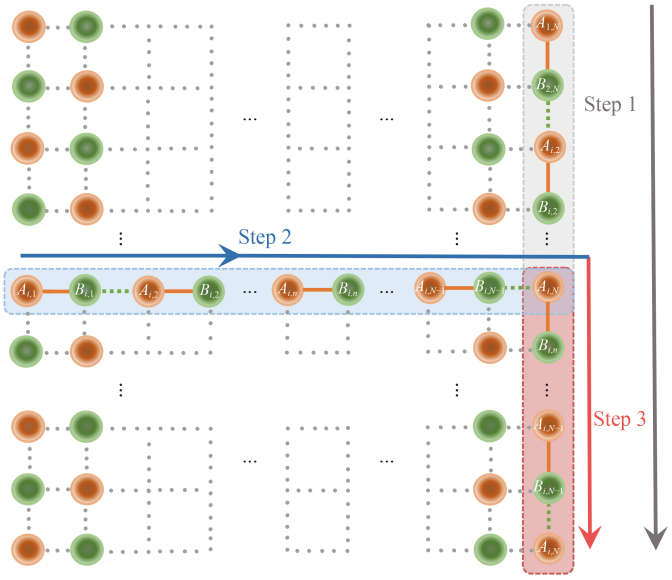

Fig. 13 The diagrammatic sketch of two-dimensional square lattice with the size of $L \times L$ in superconducting qutrit-resonator system. N-body GHZ state is generated by the ith line and the $(2N-1)$th column of SSH chain, including three steps: (i) Initialize from the qutrit $A_{1,N}$ to $A_{N,N}$ in the $(2N-1)$th column of SSH chain; (ii) The fast topological pumping from the qutrit $A_{i,1}$ to $A_{i,N}$ in the ith line of SSH chain; (iii) The fast topological pumping from the qutrit $A_{i,N}$ to $A_{N,N}$ in the $(2N-1)$th column of SSH chain.

steps:

Step 1 The $(2N-1)$th column of SSH chain is initialized in the state $|\Psi_{N,L}\rangle = (|G\rangle_{N,L} + |M\rangle_{N,L})/\sqrt{2}$, where $|G\rangle_{N,L} = |RLR\cdots\rangle_{A_{N,N}} \otimes |000\cdots\rangle_{B_{N-1,N}}$ and $|M\rangle_{N,L} = |LRL\cdots LLRLR\cdots m\rangle_{A_{N,N}} \otimes |000\cdots 0\rangle_{B_{N-1,N}}$. In particular, it is supposed that the states of the qutrit $A_{i-1,N}$ and the qutrit $A_{i,N}$ are $|L\rangle_{A_{i-1,N}}$ and $|L\rangle_{A_{i,N}}$, respectively. It is noted that such a special initial state can be represented by $|\Psi_{N,L}\rangle = |\Psi^1_{N,L}\rangle \otimes |\Psi^2_{N,L}\rangle$, where $|\Psi^1_{N,L}\rangle = (|RLR\cdots RLR\rangle_{A_{i-1,N}} + |LRL\cdots LRL\rangle_{A_{i-1,N}}) \otimes |000\cdots\rangle_{B_{i-2,N-1}}/\sqrt{2}$ is exactly an $(i-1)$-body GHZ state that can be attained by fast topological pumping in 1D SSH chain and $|\Psi^2_{N,L}\rangle = |LRL\cdots m\rangle_{A_{i,N}} \otimes |000\cdots\rangle_{B_{i,N-1}}$.

Step 2 The topological protected zero-mode state transfer occurs from the qutrit $A_{i,1}$ to the qutrit $A_{i,N}$ along the ith line of SSH chain. Initially, we suppose that the state of the ith line of SSH chain is $|l\rangle_{i,L}$, whose evolution process takes form of

$$|l\rangle_{i,L} \longrightarrow -(-1)^i |r\rangle_{i,L}, \tag{16}$$

where $|l\rangle_{i,L} = |eLR\cdots m\rangle_{A_{i,N}} \otimes |000\cdots 0\rangle_{B_{i,N-1}}$ and $|r\rangle_{i,L} = |LRL\cdots e\rangle_{A_{i,N}} \otimes |000\cdots 0\rangle_{B_{i,N-1}}$.

Step 3 Owing to the fast topological pumping from *Step 1*, the state of the $(2N-1)$th column of SSH chain is $|\Psi'_{N,L}\rangle = (|G\rangle_{N,L} + |M'\rangle_{N,L})/\sqrt{2}$, where $|M'\rangle_{N,L} = |LRL\cdots LeRLR\cdots m\rangle_{A_{1,N}} \otimes |000\cdots 0\rangle_{B_{N-1,N}}$. Subsequently, the topological protected channel is established from the qutrit $A_{i,N}$ to the qutrit $A_{N,N}$ in the $(2N-1)$th column of SSH chain, whose evolution process is followed by

$$\begin{aligned} |G\rangle_{N,L} &\longrightarrow |G\rangle_{N,L}, \\ |M'\rangle_{N,L} &\longrightarrow -(-1)^N |r\rangle_{N,L}, \end{aligned} \tag{17}$$

where $|r\rangle_{N,L} = |LRL\cdots e\rangle_{A_{i,N}} \otimes |000\cdots 0\rangle_{B_{i,N-1}}$.

Consequently, we specify that logical states 0 and 1 are carried by the ground levels $|L\rangle$ and $|R\rangle$, respectively, for the qutrit $A_{i,N}$ $(1 \le i \le N-1)$ and the zero-photon product state of resonators are discarded, which can also generate N-body GHZ state (14) in two-dimensional square lattice of superconducting qutrit-resonator system.

4 Experiment consideration for superconducting circuit devices

This protocol for generating large-scale GHZ states is applicable to superconducting circuit devices, which is benefit from existing circuit-QED technologies. We can construct a superconducting qutrit-resonator chain to arrange alternately the LC resonators and the flux qutrits in one-dimensional space, whose equivalent circuit of one unit cell is shown in Fig. 14. The flux

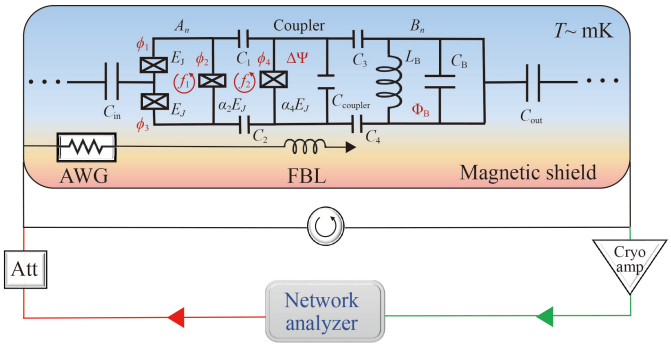

Fig. 14 Equivalent circuit of one unit cell in superconducting qutrit-resonator chain. Circuit elements are used to model the three-junction flux qutrit A_n the LC resonator B_n and the coupler with the additional Josephson junction and the coupler capacitor mounted in a dilution refrigerator (with a temperature $T \sim$ mK). The probe microwave signal is sent from a network analyzer and attenuated in the signal input line before arriving at the sample, which is placed in a magnetic shield. The transmitted signal from the sample is amplified by cryogenic LNA and measured by the network analyzer. The resonator B_n is an LC circuit composed of a spiral inductor L_B and a capacitor C_B. A flux qutrit A_n consists of a superconducting loop interrupted by three Josephson junctions. The flux qutrit A_n and the LC resonator B_n are coupled to the coupler by the capacitor $C_{1,2}$ and $C_{3,4}$, respectively. The coupling strength can be adjusted independently via changing the magnetic flux $\Delta\Psi$ threading on the loop of coupler, which can add the flux basis line (FBL) to connect with an AWG by adopting controlled voltage pulses.

qutrit A_n consists of a superconducting loop interrupted by two large Josephson junctions $E_1 = E_3 = E_J$ and one small Josephson junction $E_2 = \alpha_2 E_J$. This kind of qutrit based on three junctions enables a reduction of the loop size while retaining a large inductance [109, 110]. To create a double-well potential, $0.6 < \alpha_2 < 0.7$ is used to avoid effects of charge noise. The additional Josephson junction and the additional coupler capacitor parallel with the flux qutrit A_n and the resonator B_n, which acts as a tunable coupler with one junction E_4 controlled by the external flux-bias line (FBL) to modify the coupler properties [111–113]. The resonator B_n is composed by a spiral inductor L_B and a capacitor C_B in analogy with LC harmonic oscillator, which has a single mode. In terms of the capacitor charge Q and the inductor current I, the Hamiltonian of LC oscillator is written as

$$H_{\rm LC} = \frac{Q^2}{2C_B} + \frac{\Phi_B^2}{2L_B}, \tag{18}$$

where Φ_B is the flux through the inductor and Q the charge on the capacitor. Based on the standard quantization process of an LC circuit [105], the Hamiltonian of the resonator B_n can be further written as $H_{\rm LC} = \hbar\omega_{b_n} b_n^\dagger b_n$ in terms of the creation and annihilation operators defined by $b_n^\dagger = 1/\sqrt{2\hbar\omega_{b_n}}(Q/\sqrt{C_B} - {\rm i}\Phi_B/\sqrt{L_B})$ and $b_n = 1/\sqrt{2\hbar\omega_{b_n}}(Q/\sqrt{C_B} + {\rm i}\Phi_B/\sqrt{L_B})$, where $\omega_{b_n} = 1/\sqrt{L_B C_B}$ is the oscillator frequency and can be engineered in a large range of possible values by adjusting the parameters L_B and C_B.

At the same time, the electric dipole interaction between the flux qutrit A_n and the resonator B_n can be realized by using a tunable coupler without considering the charge interaction [114]. A more versatile design, shown in Fig. 14, separates the three-junction flux qutrit and the resonator by an additional Josephson junction, while keeping the flux qutrits quantization independent of an additional flux difference along the segment $\Delta\Psi$, which is the source of the coupling. The corresponding Hamiltonian for the three-junction flux qutrit and the additional Josephson junction is [111, 115, 116]

$$H_{\rm q} = \frac{P_p^2}{2M_p} + \frac{P_m^2}{2M_m} + U_{\rm eff}, \tag{19}$$

where $M_p = 2C_J[\Phi_0/(2\pi)]^2$ and $M_m = M_p(1+2\alpha)$ can be considered effective masses, while $P_p = -{\rm i}\hbar\partial/\partial\phi_p$ and $P_m = -{\rm i}\hbar\partial/\partial\phi_m$ can be considered effective momenta. Moreover, $\phi_p = (\phi_1 + \phi_3 + \phi_2)/2$ and $\phi_m = (\phi_1 + \phi_3 - \phi_2)/2$ are defined by the phase drops ϕ_n across the junction E_{j_n} $(n = 1, 2, 3)$. The effective potential of flux qutrit and the additional Josephson junction is given by $U_{\rm eff} = E_J\,[-\alpha_2\,\cos(f_1 - \phi_p) - 2\cos(\phi_m/2)\,\cos(\phi_p/2)] + \alpha_4\,E_J\,\cos(f_1 + f_2 - \Delta\Psi + \phi_p)$, where α_4 is the ratio of the added Josephson junction energy E_4 to the larger Josephson junction energy E_J and f_n $(n = 1, 2)$ reduced magnetic flux through the loop n. When $f_1 \neq 0.5$, a flux qutrit holds a Λ-type energy level structure [117, 118]. When introducing the capacitive terms from the coupler capacitive $C_{\rm coupler}$, a numerical evaluation of the Hamiltonian for $f_2 = \pi$ in the qutrit basis reveals that

$$H_{\rm q} \sim \sum_{k=L,R,e} \Delta_k |k\rangle\langle k| + \alpha_4 E_J \Delta\Psi \sum_{m=L,R} c_r^1(\alpha_2, \alpha_4, f_1)\sigma_m, \tag{20}$$

where Δ_k the frequency of the energy $|k\rangle$ in the qutrit A_n and $\sigma_m = |m\rangle_n\langle e| + |e\rangle_n\langle m|$ $(m = L, R)$. $c_m^1(\alpha_2, \alpha_4, f_1)$ is liner in the field and has a tunable orientation. To be specific, the explicit expression of the function can be represented by $c_r^1(\alpha_2, \alpha_4, f_1) = \sin(f_1 + \phi_+)$, where $\phi_+ = \phi_1 + \phi_3$ and $f_1 = \phi_1 + \phi_3 - \phi_2 - \phi_4$. The phases ϕ_n across the junction E_n $(n = 1, 2, 3, 4)$ are strongly associated with the values of α_2 and α_4 [114]. Accordingly, we restrict to the case in which the line forms a single-mode resonator B_n and the phase slip then becomes approximately

$$\begin{aligned}\Delta\Psi &= \frac{\partial_x u(\boldsymbol{x})\Delta x}{\phi_0}\sqrt{\frac{\hbar}{\omega_{b_n} C}}(b_n + b_n^\dagger) \\ &= \frac{2\pi\partial_x\Psi(\boldsymbol{x})\Delta x}{\Phi_0}(b_n + b_n^\dagger),\end{aligned} \tag{21}$$

where $u(\boldsymbol{x})$ is the photon mode eigenfunction in the resonator, Δx the separation between the two qutrit-line intersections and C the total transmission line capacitance. Assuming a flux gradient $|\partial_x\Psi(\boldsymbol{x})| = 65\times 10^{-5}\Phi_0$ μm and a qutrit size $\Delta x = 5$ μm, we reach a coupling $J_0 = 2\times 10^{-4} E_J$, which for a typical junction with $E_J = 250$ GHz implies a 50 MHz coupling. By substituting quantized magnetic flux and employing the rotating wave approximation in the qutrit-resonator chain, the quantized interaction Hamiltonian can be obtained in Eq. (1).

Notice that the coupling term is strictly independent of the qutrit Hamiltonian, so it now becomes possible to switch on and off the interaction. The simplest way to tune the coupling strength $J_{1,2}$ is to apply a control magnetic flux to this loop dynamically with $\Psi(\boldsymbol{x}) = \int_s \boldsymbol{B}(\boldsymbol{x}, t)\cdot {\rm d}\boldsymbol{S}$, by adding the FBL to connect with an arbitrary waveforms generator (AWG) by adopting controlled voltage pulses [119], shown in Fig. 14. Moreover, the coupling between the flux qutrit and the resonator induced by the capacitive energy of junctions gives a negligible coupling $\sim 10^{-3}\hbar\omega_{b_n}$ [111]. It is an expedient way to add one additional Josephson junction indicating that (i) the tunable couplings between the qutrit and the resonator can switch on and off by the parameter f_1 in contrast to no additional Josephson junction and (ii) the complexity of superconducting circuits and unexpected higher-order couplings can be reduced by adding less number of Josephson junctions.

In addition, an appropriate flux difference increasing or decreasing f_1 is applied on the flux qutrit A_1 to unbalance the populations of the two current states and create a superposition state of $(|R\rangle + |e\rangle)/\sqrt{2}$ [120]. The resonator stays in the zero-photon Fock state. Finally, the qutrit-resonator chain can be prepared in $1/\sqrt{2}(|RLR\cdots R(L)\rangle_{A_N} + |eLR\cdots R(L)\rangle_{A_N}) \otimes |000\cdots 0\rangle_{B_{N-1}}$.

In experiment, the above superconducting circuit device can be integrated by a metal chip, which is fabricated on a micron scale and operated in the dilution refrigerator at millikelvin temperatures [119, 121–123]. These circuits are driven by currents, voltages and microwave photons that excite the system from one quantum state to another in a controllable manner, which can be used to test fundamental quantum mechanical principles at a macroscopic scale. As shown in Fig. 14, the probe microwave signal is continuously sent from a network analyzer and attenuated in the signal input line before arriving at the sample, which is placed in a magnetic shield. The transmitted signal from the sample is amplified and measured by the network analyzer. Furthermore, the superconducting quantum computer on the order of 65-qubit has been realized [124]. The 72-site circuit QED lattice was demonstrated experimentally [30]. Thus, superconducting circuits possessing advantages of flexibility, scalability and tunability [18, 125, 126], provide an excellent platform for generating large-scale GHZ states with a high fidelity.

5 Conclusion

Summing up, we have proposed the scheme of the fast topological pumping via edge channels with respect to a single excitation to generate large-scale GHZ states in a generalized SSH model of a superconducting qutrit-resonator circuit. We analytically derive that this generalized SSH model can be expressed as a two-band structure in momentum space, and its topologically trivial and nontrivial phase can be characterized by Zak phase equal to 0 and π, respectively. There is a nontrivial band gap to protect fast topological pumping via edge channels. The crucial characteristics of exponential couplings for fast topological pumping are that it suitably adapts the slope of the coupling functions based on the value of the instantaneous energy gap, while at the same time it ensures that the minimum value of the energy gap is as greater as possible. We study the effect of the disorder and losses of system for generating large-scale GHZ states, emphasizing the fact that the robustness of large-scale GHZ state are increased. Furthermore, the accessible scalability of entanglement based on the fast topological pumping outperforms a lot the conventional adiabatic topological pumping. Last but not least, the multiple platforms for realization of the fast topological pumping in experimental setups may mitigate additional constraints and possibilities for the control with respect to the other accelerating methods [11–13, 55]. The scheme provides a fast topological pumping to generate large-scale GHZ states with high fidelity and robustness, which is expected to make a substantial contribution to speeding up adiabatic protocols with the topological properties of matter in the superconducting circuit device.

Acknowledgements This work was supported by the National Natural Science Foundation of China (Grant No. 11675046), the Program for Innovation Research of Science in Harbin Institute of Technology (Grant No. A201412), and the Postdoctoral Scientific Research Developmental Fund of Heilongjiang Province (Grant No. LBH-Q15060).

Appendix A Derivation of zero-mode edge state

For the odd-sized superconducting qutrit-resonator chain, the translational invariance of the system suggests the following ansatz for an eigenstate of edge state

$$|\varphi_E\rangle = \sum_{n=1}^{N} \lambda^n \Big[\gamma\sigma_n^\dagger(\sigma_n^x)^{n-1}\bigotimes_{l=1}^{n-1}\sigma_l^x + \eta b_n^\dagger\bigotimes_{l=1}^{n}\sigma_l^x\Big]|G\rangle_L, \tag{A1}$$

where $\sigma_n^+ = |e\rangle_n\langle R|$ and $|G\rangle_L = |RLR\cdots\rangle_{A_N}\otimes|000\cdots\rangle_{B_{N-1}}$ denotes a decoupled state of the qutrit-resonator chain by mapping into the parameter coordinate space with A_1 in $|R\rangle$, B_1 in $|0\rangle$ (zero-photon Fock state), A_2 in $|L\rangle$, B_2 in $|0\rangle$, ... λ is the localized index, γ and η being the probability amplitude of the gap states. The probability amplitude on site n decays (increases) exponentially with the distance n when $|\lambda| < 1$ ($|\lambda| > 1$), corresponding to the left (right) edge state, after the wave function is normalized. It is supposed that the eigenenergy of an edge state is E. Through the eigenvalue equation $E|\varphi_E\rangle = H_{2N-1}|\varphi_E\rangle$, one can obtain

$$\begin{aligned}
&E\sum_{n=1}^{N}\lambda^n\Big[\gamma\sigma_n^\dagger(\sigma_n^x)^{n-1}\bigotimes_{l=1}^{n-1}\sigma_l^x + \eta b_n^\dagger\bigotimes_{l=1}^{n}\sigma_l^x\Big]|G\rangle_L \\
&= J_1\lambda^n\Big[\eta\sigma_n^\dagger(\sigma_n^x)^n\bigotimes_{l=1}^{n}\sigma_l^x + \gamma b_n^\dagger\bigotimes_{l=1}^{n}\sigma_l^x\Big]|G\rangle_L \\
&\quad + J_2\Big[\eta\lambda^{n-1}\sigma_n^\dagger(\sigma_n^x)^{n-1}\bigotimes_{l=1}^{n-1}\sigma_l^x + \gamma\lambda^{n+1}b_j^\dagger\bigotimes_{l=1}^{n}\sigma_l^x\Big]|G\rangle_L.
\end{aligned} \tag{A2}$$

When $\gamma = 0$ ($\eta = 0$), according to Eq. (A1) the resonators (qutrits) are occupied by the edge state whose eigenenergy is $E = 0$. In particular, in order to

generate large-scale GHZ states of qutrits, we choose $\gamma = 1$ and $\eta = 0$ to render the qutrit in each unit cell to occupy the left ($\lambda < 1$) and right ($\lambda > 1$) edge states with $E = 0$. Then, the edge state wave function can be derived as

$$|\varphi_E\rangle = \sum_{n=1}^{N} \lambda^n \sigma_n^{\dagger} (\sigma_n^x)^{n-1} \bigotimes_{l=1}^{n-1} \sigma_l^x |G\rangle_L, \tag{A3}$$

with $\lambda = -J_1/J_2$.

References

1. A. Y. Kitaev, Unpaired Majorana fermions in quantum wires, *Phys. Uspekhi.* 44(103), 131 (2001)
2. C. L. Kane and E. J. Mele, Z_2 topological order and the quantum spin Hall effect, *Phys. Rev. Lett.* 95(14), 146802 (2005)
3. D. J. Thouless, Quantization of particle transport, *Phys. Rev. B* 27(10), 6083 (1983)
4. Q. Niu and D. J. Thouless, Quantised adiabatic charge transport in the presence of substrate disorder and many-body interaction, *J. Phys. Math. Gen.* 17(12), 2453 (1984)
5. Y. E. Kraus, Y. Lahini, Z. Ringel, M. Verbin, and O. Zilberberg, Topological states and adiabatic pumping in quasicrystals, *Phys. Rev. Lett.* 109(10), 106402 (2012)
6. M. Verbin, O. Zilberberg, Y. Lahini, Y. E. Kraus, and Y. Silberberg, Topological pumping over a photonic Fibonacci quasicrystal, *Phys. Rev. B* 91(6), 064201 (2015)
7. N. Lang and H. P. Büchler, Topological networks for quantum commuication between distant qubits, *npj Quantum Inf.* 3, 47 (2017)
8. F. Mei, G. Chen, L. Tian, S. L. Zhu, and S. Jia, Robust quantum state transfer via topological edge states in superconducting qubit chains, *Phys. Rev. A* 98(1), 012331 (2018)
9. J. L. Tambasco, G. Corrielli, R. J. Chapman, A. Crespi, O. Zilberberg, R. Osellame, and A. Peruzzo, Quantum interference of topological states of light, *Sci. Adv.* 4(9), eaat3187 (2018)
10. P. Boross, J. K. Asbóth, G. Széchenyi, L. Oroszlány, and A. Pályi, Poor man's topological quantum gate based on the Su–Schrieffer–Heeger model, *Phys. Rev. B* 100(4), 045414 (2019)
11. S. Longhi, Topological pumping of edge states via adiabatic passage, *Phys. Rev. B* 99(15), 155150 (2019)
12. N. E. Palaiodimopoulos, I. Brouzos, F. K. Diakonos, and G. Theocharis, Fast and robust quantum state transfer via a topological chain, *Phys. Rev. A* 103(5), 052409 (2021)
13. F. M. D'Angelis, F. A. Pinheiro, D. Guéry-Odelin, S. Longhi, and F. Impens, Fast and robust quantum state transfer in a topological Su–Schrieffer–Heeger chain with next-to-nearest-neighbor interactions, *Phys. Rev. Res.* 2(3), 033475 (2020)
14. F. Mei, G. Chen, L. Tian, S. L. Zhu, and S. Jia, Topology-dependent quantum dynamics and entanglement-dependent topological pumping in superconducting qubit chains, *Phys. Rev. A* 98(3), 032323 (2018)
15. J. X. Han, J. L. Wu, Y. Wang, Y. Xia, Y. Y. Jiang, and J. Song, Large-scale Greenberger–Horne–Zeilinger states through a topologically protected zero-energy mode in a superconducting qutrit-resonator chain, *Phys. Rev. A* 103(3), 032402 (2021)
16. S. Das Sarma, M. Freedman, and C. Nayak, Topological quantum computation, *Phys. Today* 59(7), 32 (2006)
17. M. H. Devoret, and R. J. Schoelkopf, Superconducting circuits for quantum information: An outlook, *Science* 339(6124), 1169 (2013)
18. J. Q. You and F. Nori, Atomic physics and quantum optics using superconducting circuits, *Nature* 474(189), 8 (2005)
19. J. M. Martinis, Qubit metrdogy for building a fault–tolerant quantum computer, *npj Quantum Inf.* 1, 15005 (2015)
20. C. Song, K. Xu, H. Li, Y. R. Zhang, X. Zhang, W. Liu, Q. Guo, Z. Wang, W. Ren, J. Hao, H. Feng, H. Fan, D. Zheng, D. W. Wang, H. Wang, and S. Y. Zhu, Generation of multicomponent atomic Schrödinger cat states of up to 20 qubits, *Science* 365(6453), 574 (2019)
21. J. Kelly, R. Barends, A. G. Fowler, A. Megrant, E. Jeffrey, T. C. White, D. Sank, J. Y. Mutus, B. Campbell, Y. Chen, Z. Chen, B. Chiaro, A. Dunsworth, I. C. Hoi, C. Neill, P. J. J. O'Malley, C. Quintana, P. Roushan, A. Vainsencher, J. Wenner, A. N. Cleland, and J. M. Martinis, State preservation by repetitive error detection in a superconducting quantum circuit, *Nature* 519(7541), 66 (2015)
22. J. S. Otterbach, R. Manenti, N. Alidoust, A. Bestwick, M. Block, B. Bloom, S. Caldwell, N. Didier, E. S. Fried, S. Hong, P. Karalekas, C. B. Osborn, A. Papageorge, E. C. Peterson, G. Prawiroatmodjo, N. Rubin, C. A. Ryan, D. Scarabelli, M. Scheer, E. A. Sete, P. Sivarajah, R. S. Smith, N. T. A. Staley, W. J. Zeng, A. Hudson, B. R. Johnson, M. Reagor, M. P. da Silva, and C. Rigetti, Unsupervised machine learning on a hybrid quantum computer, arXiv: 1712.05771 (2017)
23. A. Kandala, A. Mezzacapo, K. Temme, M. Takita, M. Brink, J. M. Chow, and J. M. Gambetta, Hardware-efficient variational quantum eigensolver for small molecules and quantum magnets, *Nature* 549(7671), 242 (2017)
24. C. Neill, P. Roushan, K. Kechedzhi, S. Boixo, S. V. Isakov, V. Smelyanskiy, A. Megrant, B. Chiaro, A. Dunsworth, K. Arya, R. Barends, B. Burkett, Y. Chen, Z. Chen, A. Fowler, B. Foxen, M. Giustina, R. Graff, E. Jeffrey, T. Huang, J. Kelly, P. Klimov, E. Lucero, J. Mutus, M. Neeley, C. Quintana, D. Sank, A. Vainsencher, J. Wenner, T. C. White, H. Neven, and J. M. Martinis, A blueprint for demonstrating quantum supremacy with superconducting qubits, *Science* 360(6385), 195 (2018)
25. K. X. Wei, I. Lauer, S. Srinivasan, N. Sundaresan, D. T. McClure, D. Toyli, D. C. McKay, J. M. Gambetta, and S. Sheldon, Verifying multipartite entangled Greenberger–Horne–Zeilinger states via multiple quantum coherences, *Phys. Rev. A* 101(3), 032343 (2020)

26. Y. Salathé, M. Mondal, M. Oppliger, J. Heinsoo, P. Kurpiers, A. Potočnik, A. Mezzacapo, U. Las Heras, L. Lamata, E. Solano, S. Filipp, and A. Wallraff, Digital quantum simulation of spin models with circuit quantum electrodynamics, *Phys. Rev. X* 5(2), 021027 (2015)
27. S. Hacohen-Gourgy, V. V. Ramasesh, C. De Grandi, I. Siddiqi, and S. M. Girvin, Cooling and autonomous feedback in a Bose–Hubbard chain with attractive interactions, *Phys. Rev. Lett.* 115(24), 240501 (2015)
28. P. J. J. O'Malley, R. Babbush, I. D. Kivlichan, J. Romero, J. R. McClean, R. Barends, J. Kelly, P. Roushan, A. Tranter, N. Ding, B. Campbell, Y. Chen, Z. Chen, B. Chiaro, A. Dunsworth, A. G. Fowler, E. Jeffrey, E. Lucero, A. Megrant, J. Y. Mutus, M. Neeley, C. Neill, C. Quintana, D. Sank, A. Vainsencher, J. Wenner, T. C. White, P. V. Coveney, P. J. Love, H. Neven, A. Aspuru-Guzik, and J. M. Martinis, Scalable quantum simulation of molecular energies, *Phys. Rev. X* 6(3), 031007 (2016)
29. Y. P. Zhong, D. Xu, P. Wang, C. Song, Q. J. Guo, W. X. Liu, K. Xu, B. X. Xia, C. Y. Lu, S. Han, J. W. Pan, and H. Wang, Emulating anyonic fractional statistical behavior in a superconducting quantum circuit, *Phys. Rev. Lett.* 117(11), 110501 (2016)
30. M. Fitzpatrick, N. M. Sundaresan, A. C. Y. Li, J. Koch, and A. A. Houck, Observation of a dissipative phase transition in a one-dimensional circuit QED lattice, *Phys. Rev. X* 7(1), 011016 (2017)
31. J. Q. You, X. F. Shi, X. Hu, and F. Nori, Quantum emulation of a spin system with topologically protected ground states using superconducting quantum circuits, *Phys. Rev. B* 81(1), 014505 (2010)
32. J. Koch, A. A. Houck, K. L. Hur, and S. M. Girvin, Time–reversal-symmetry breaking in circuit-QED-based photon lattices, *Phys. Rev. A* 82(4), 043811 (2010)
33. M. Hafezi, P. Adhikari, and J. M. Taylor, Engineering three-body interaction and Pfaffian states in circuit QED systems, *Phys. Rev. B* 90(6), 060503 (2014)
34. E. Kapit, M. Hafezi, and S. H. Simon, Induced self-stabilization in fractional quantum Hall states of light, *Phys. Rev. X* 4(3), 031039 (2014)
35. D. I. Tsomokos, S. Ashhab, and F. Nori, Using superconducting qubit circuits to engineer exotic lattice systems, *Phys. Rev. A* 82(5), 052311 (2010)
36. F. Mei, Z. Y. Xue, D. W. Zhang, L. Tian, C. Lee, and S. L. Zhu, Witnessing topological Weyl semimetal phase in a minimal circuit-QED lattice, *Quantum Sci. Technol.* 1(1), 015006 (2016)
37. J. Tangpanitanon, V. M. Bastidas, S. Al-Assam, P. Roushan, D. Jaksch, and D. G. Angelakis, Topological pumping of photons in nonlinear resonator arrays, *Phys. Rev. Lett.* 117(21), 213603 (2016)
38. T. Goren, K. Plekhanov, F. Appas, and K. Le Hur, Topological Zak phase in strongly coupled LC circuits, *Phys. Rev. B* 97(4), 041106 (2018)
39. V. V. Ramasesh, E. Flurin, M. Rudner, I. Siddiqi, and N. Y. Yao, Direct probe of topological invariants using Bloch oscillating quantum walks, *Phys. Rev. Lett.* 118(13), 130501 (2017)
40. E. Flurin, V. V. Ramasesh, S. Hacohen-Gourgy, L. S. Martin, N. Y. Yao, and I. Siddiqi, Observing topological invariants using quantum walks in superconducting circuits, *Phys. Rev. X* 7(3), 031023 (2017)
41. M. D. Schroer, M. H. Kolodrubetz, W. F. Kindel, M. Sandberg, J. Gao, M. R. Vissers, D. P. Pappas, A. Polkovnikov, and K. W. Lehnert, Measuring a topological transition in an artificial spin-1/2 system, *Phys. Rev. Lett.* 113(5), 050402 (2014)
42. P. Roushan, C. Neill, Y. Chen, M. Kolodrubetz, C. Quintana, N. Leung, M. Fang, R. Barends, B. Campbell, Z. Chen, B. Chiaro, and A. Dunsworth, E. Jeffrey, J. Kelly, A. Megrant, J. Mutus, P. J. J. O'Malley, D. Sank, A. Vainsencher, J. Wenner, T. White, A. Polkovnikov, A. N. Cleland, and J. M. Martinis, Observation of topological transitions in interacting quantum circuits, *Nature* 515(7526), 241 (2014)
43. Z. Zhang, T. Wang, L. Xiang, J. Yao, J. Wu, and Y. Yin, Measuring the Berry phase in a superconducting phase qubit by a shortcut to adiabaticity, *Phys. Rev. A* 95(4), 042345 (2017)
44. X. Tan, D. W. Zhang, Q. Liu, G. Xue, H. F. Yu, Y. Q. Zhu, H. Yan, S. L. Zhu, and Y. Yu, Topological Maxwell metal bands in a superconducting qutrit, *Phys. Rev. Lett.* 120(13), 130503 (2018)
45. C. Song, D. Xu, P. Zhang, J. Wang, Q. Guo, W. Liu, K. Xu, H. Deng, K. Huang, D. Zheng, S. B. Zheng, H. Wang, X. Zhu, C. Y. Lu, and J. W. Pan, Demonstration of topological robustness of anyonic braiding statistics with a superconducting quantum circuit, *Phys. Rev. Lett.* 121(3), 030502 (2018)
46. W. Cai, J. Han, F. Mei, Y. Xu, Y. Ma, X. Li, H. Wang, Y. P. Song, Z. Y. Xue, Z. Q. Yin, S. Jia, and L. Sun, Observation of topological magnon insulator states in a superconducting circuit, *Phys. Rev. Lett.* 123(8), 080501 (2019)
47. O. Viyuela, A. Rivas, S. Gasparinetti, A. Wallraff, A. Wallraff, S. Filipp, and M. A. Martin-Delgado, Observation of topological Uhlmann phases with superconduction qubits, *npj Quantum Inform.* 4, 10 (2018)
48. R. Horodecki, P. Horodecki, M. Horodecki, and K. Horodecki, Quantum entanglement, *Rev. Mod. Phys.* 81(2), 865 (2009)
49. J. W. Pan, Z. B. Chen, C. Y. Lu, H. Weinfurter, A. Zeilinger, and M. Żukowski, Multiphoton entanglement and interferometry, *Rev. Mod. Phys.* 84(2), 777 (2012)
50. L. Pezzè, A. Smerzi, M. K. Oberthaler, R. Schmied, and P. Treutlein, Quantum metrology with nonclassical states of atomic ensembles, *Rev. Mod. Phys.* 90(3), 035005 (2018)
51. M. C. Rechtsman, Y. Lumer, Y. Plotnik, A. Perez-Leija, A. Szameit, and M. Segev, Topological protection of photonic path entanglement, *Optica* 3(9), 925 (2016)
52. A. Blanco-Redondo, B. Bell, D. Oren, B. J. Eggleton, and M. Segev, Topological protection of biphoton states, *Science* 362(6414), 568 (2018)
53. M. Wang, C. Doyle, B. Bell, M. J. Collins, E. Magi, B. J. Eggleton, M. Segev, and A. Blanco-Redondo, Topologically protected entangled photonic states, *Nanophotonics* 8(8), 1327 (2019)
54. C. K. Hong, Z. Y. Ou, and L. Mandel, Measurement of subpicosecond time intervals between two photons by interference, *Phys. Rev. Lett.* 59(18), 2044 (1987)
55. I. Brouzos, I. Kiorpelidis, F. K. Diakonos, and G.

Theocharis, Fast, robust, and amplified transfer of topological edge modes on a time-varying mechanical chain, *Phys. Rev. B* 102(17), 174312 (2020)
56. Y. X. Shen, L. S. Zeng, Z. G. Geng, D. G. Zhao, Y. G. Peng, and X. F. Zhu, Acoustic adiabatic propagation based on topological pumping in a coupled multicavity chain lattice, *Phys. Rev. Appl.* 14(1), 014043 (2020)
57. J. L. Wu, Y. Wang, J. X. Han, Y. K. Feng, S. L. Su, Y. Xia, Y. Jiang, and J. Song, One-step implementation of Rydberg-antiblockade SWAP and controlled-SWAP gates with modified robustness, *Photon. Res.* 9(5), 814 (2021)
58. X. R. Huang, Z. X. Ding, C. S. Hu, L. T. Shen, W. Li, H. Wu, and S. B. Zheng, Robust Rydberg gate via Landau–Zener control of Förster resonance, *Phys. Rev. A* 98(5), 052324 (2018)
59. Q. Guo, S. B. Zheng, J. Wang, C. Song, P. Zhang, K. Li, W. Liu, H. Deng, K. Huang, D. Zheng, X. Zhu, H. Wang, C. Y. Lu, and J. W. Pan, Dephasing-insensitive quantum information storage and processing with superconducting qubits, *Phys. Rev. Lett.* 121(13), 130501 (2018)
60. V. Balachandran and J. Gong, Adiabatic quantum transport in a spin chain with a moving potential, *Phys. Rev. A* 77(1), 012303 (2008)
61. J. Allcock and N. Linden, Quantum communication beyond the localization length in disordered spin chains, *Phys. Rev. Lett.* 102(11), 110501 (2009)
62. J. L. Wu, Y. Wang, J. X. Han, S. L. Su, Y. Xia, Y. Jiang, and J. Song, Unselective ground-state blockade of Rydberg atoms for implementing quantum gates, *Front. Phys.* 17(2), 22501 (2022)
63. R. R. Agundez, C. D. Hill, L. C. L. Hollenberg, S. Rogge, and M. Blaauboer, Superadiabatic quantum state transfer in spin chains, *Phys. Rev. A* 95(1), 012317 (2017)
64. J. L. Wu, Y. Wang, J. X. Han, Y. Jiang, J. Song, Y. Xia, S. L. Su, and W. Li, Systematic-error-tolerant multiqubit holonomic entangling gates, *Phys. Rev. Appl.* 16(6), 064031 (2021)
65. Y. Zhou, D. Y. Lü, and W. Y. Zeng, Chiral single-photon switch-assisted quantum logic gate with a nitrogen-vacancy center in a hybrid system, *Photon. Res.* 9(3), 405 (2021)
66. D. M. Greenberger, M. A. Horne, and A. Zeilinger, Bell's theorem, Quantum Theory, and Conceptions of the Universe, Kluwer Dordrecht, 1989
67. M. Hillery, V. Bužek, and A. Berthiaume, Quantum secret sharing, *Phys. Rev. A* 59(3), 1829 (1999)
68. S. Bose, V. Vedral, and P. L. Knight, Multiparticle generalization of entanglement swapping, *Phys. Rev. A* 57(2), 822 (1998)
69. E. Knill, Quantum computing with realistically noisy devices, *Nature* 434(7029), 39 (2005)
70. V. Giovannetti, S. Lloyd, and L. Maccone, Quantum-enhanced measurements: Beating the standard quantum limit, *Science* 306(5700), 1330 (2004)
71. D. Leibfried, M. Barrett, T. Schaetz, J. Britton, J. Chiaverini, W. Itano, J. Jost, C. Langer, and D. Wineland, Toward Heisenberg-limited spectroscopy with multiparticle entangled states, *Science* 304(5676), 1476 (2004)
72. C. P. Yang, Q. P. Su, S. B. Zheng, and F. Nori, Entangling superconducting qubits in a multi-cavity system, *New J. Phys.* 18(1), 013025 (2016)
73. S. Matsuo, S. Ashhab, T. Fujii, F. Nori, K. Nagai, and N. Hatakenaka, Generation of Bell states and Greenberger–Horne–Zeilinger states in superconducting phase qubits, in: Quantum Communication, Measurement and Computing, No. 8, Ed.: O. Hirota *et al.*, Tokyo: NICT, 2006
74. L. F. Wei, Y. Liu, and F. Nori, Generation and control of Greenberger–Horne–Zeilinger entanglement in superconducting circuits, *Phys. Rev. Lett.* 96(24), 246803 (2006)
75. S. L. Zhu, Z. D. Wang, and P. Zanardi, Geometric quantum computation and multiqubit entanglement with superconducting qubits inside a cavity, *Phys. Rev. Lett.* 94(10), 100502 (2005)
76. C. P. Yang, Q. P. Su, and S. Han, Generation of Greenberger–Horne–Zeilinger entangled states of photons in multiple cavities via a superconducting qutrit or an atom through resonant interaction, *Phys. Rev. A* 86(2), 022329 (2012)
77. C. P. Yang, Q. P. Su, S. B. Zheng, and S. Han, Generating entanglement between microwave photons and qubits in multiple cavities coupled by a superconducting qutrit, *Phys. Rev. A* 87(2), 022320 (2013)
78. S. Aldana, Y. D. Wang, and C. Bruder, Greenberger–Horne–Zeilinger generation protocol for N superconducting transmon qubits capacitively coupled to a quantum bus, *Phys. Rev. B* 84(13), 134519 (2011)
79. W. Feng, P. Wang, X. Ding, L. Xu, and X. Q. Li, Generating and stabilizing the Greenberger–Horne–Zeilinger state in circuit QED: Joint measurement, Zeno effect, and feedback, *Phys. Rev. A* 83(4), 042313 (2011)
80. J. L. Wu, C. Song, J. Xu, L. Yu, X. Ji, and S. Zhang, Adiabatic passage for one-step generation of n-qubit Greenberger–Horne–Zeilinger states of superconducting qubits via quantum Zeno dynamics, *Quantum Inform. Process.* 15(9), 3663 (2016)
81. X. T. Mo, and Z. Y. Xue, Single-step multipartite entangled states generation from coupled circuit cavities, *Front. Phys.* 14(3), 31602 (2019)
82. Y. H. Kang, Z. C. Shi, B. H. Huang, J. Song, and Y. Xia, Deterministic conversions between Greenberger–Horne–Zeilinger states and W states of spin qubits via Lie-transform-based inverse Hamiltonian engineering, *Phys. Rev. A* 100(1), 012332 (2019)
83. T. Liu, Q. P. Su, Y. Zhang, Y. L. Fang, and C. P. Yang, Generation of quantum entangled states of multiple groups of qubits distributed in multiple cavities, *Phys. Rev. A* 101(1), 012337 (2020)
84. J. M. Chow, J. M. Gambetta, E. Magesan, D. W. Abraham, A. W. Cross, B. R. Johnson, N. A. Masluk, C. A. Ryan, J. A. Smolin, S. J. Srinivasan, and M. Steffen, Implementing a strand of a scalable fault-tolerant quantum computing fabric, *Nat. Commun.* 5(1), 4015 (2014)
85. L. DiCarlo, M. D. Reed, L. Sun, B. R. Johnson, J. M. Chow, J. M. Gambetta, L. Frunzio, and M. H. Girvin, S. M. and Devoret, and R. J. Schoelkopf, Preparation and measurement of three-qubit entanglement in a

superconduction circuit, *Nature* 467(7315), 574 (2010)
86. R. Barends, J. Kelly, A. Megrant, A. Veitia, D. Sank, E. Jeffrey, T. C. White, J. Mutus, A. G. Fowler, B. Campbell, Y. Chen, Z. Chen, B. Chiaro, A. Dunsworth, C. Neill, P. O'Malley, P. Roushan, A. Vainsencher, J. Wenner, A. N. Korotkov, A. N. Cleland, and J. M. Martinis, Superconducting quantum circuits at the surface code threshold for fault tolerance, *Nature* 508(7497), 500 (2014)
87. C. Song, K. Xu, W. Liu, C. Yang, S. B. Zheng, H. Deng, Q. Xie, K. Huang, Q. Guo, L. Zhang, P. Zhang, D. Xu, D. Zheng, X. Zhu, H. Wang, Y. A. Chen, C. Y. Lu, S. Han, and J. W. Pan, 10-qubit entanglement and parallel logic operations with a superconducting circuit, *Phys. Rev. Lett.* 119(18), 180511 (2017)
88. A. Cervera-Lierta, M. Krenn, A. Aspuru-Guzik, and A. Galda, Experimental high-dimensional Greenberger–Horne–Zeilinger entanglement with superconducting transmon qutrits, *Phys. Rev. Appl.* 17(2), 024062 (2022)
89. X. Chen, I. Lizuain, A. Ruschhaupt, D. Guéry-Odelin, and J. G. Muga, Shortcut to adiabatic passage in two- and three-level atoms, *Phys. Rev. Lett.* 105(12), 123003 (2010)
90. D. Guéry-Odelin, A. Ruschhaupt, A. Kiely, E. Torrontegui, S. Martínez-Garaot, and J. G. Muga, Shortcuts to adiabaticity: Concepts, methods, and applications, *Rev. Mod. Phys.* 91(4), 045001 (2019)
91. A. Altland and M. R. Zirnbauer, Nonstandard symmetry classes in mesoscopic normal-superconducting hybrid structures, *Phys. Rev. B* 55(2), 1142 (1997)
92. S. Ryu, and Y. Hatsugai, Topological origin of zero-energy edge states in particle–hole symmetric systems, *Phys. Rev. Lett.* 89(7), 077002 (2002)
93. J. K. Asbóth, L. Oroszlány, and A. Pályi, A short course on topological insulators, *Lect. Notes Phys.* 919, 85 (2016)
94. A. Coutant, V. Achilleos, O. Richoux, G. Theocharis, and V. Pagneux, Robustness of topological corner modes against disorder with application to acoustic networks, *Phys. Rev. B* 102(21), 214204 (2020)
95. D. M. Greenberger, M. A. Horne, A. Shimony, and A. Zeilinger, Bell's theorem without inequalities, *Am. J. Phys.* 58(12), 1131 (1990)
96. R. Mukherjee, H. Xie, and F. Mintert, Bayesian optimal control of Greenberger–Horne–Zeilinger states in Rydberg lattices, *Phys. Rev. Lett.* 125(20), 203603 (2020)
97. F. Reiter, D. Reeb, and A. S. Sørensen, Scalable dissipative preparation of many-body entanglement, *Phys. Rev. Lett.* 117(4), 040501 (2016)
98. S. B. Zheng, One-step synthesis of multiatom Greenberger–Horne–Zeilinger states, *Phys. Rev. Lett.* 87(23), 230404 (2001)
99. P. Mundada, G. Zhang, T. Hazard, and A. Houck, Suppression of qubit crosstalk in a tunable coupling superconducting circuit, *Phys. Rev. Appl.* 12(5), 054023 (2019)
100. W. P. Su, J. R. Schrieffer, and A. J. Heeger, Solitons in Polyacetylene, *Phys. Rev. Lett.* 42(25), 1698 (1979)
101. J. Pachos, and H. Walther, Quantum computation with trapped ions in an optical cavity, *Phys. Rev. Lett.* 89(18), 187903 (2002)
102. A. P. M. Place, L. V. H. Rodgers, P. Mundada, B. M. Smitham, M. Fitzpatrick, Z. Leng, A. Premkumar, J. Bryon, A. Vrajitoarea, S. Sussman, G. Cheng, T. Madhavan, H. K. Babla, X. H. Le, Y. Gang, B. Jäck, A. Gyenis, N. Yao, R. J. Cava, N. P. de Leon, and A. A. Houck, New material platform for superconducting transmon qubits with coherence times exceeding 0.3 milliseconds, *Nat. Commun.* 12(1), 1779 (2021)
103. H. Zhang, S. Chakram, T. Roy, N. Earnest, Y. Lu, Z. Huang, D. K. Weiss, J. Koch, and D. I. Schuster, Universal fast-flux control of a coherent, low-frequency qubit, *Phys. Rev. X* 11(1), 011010 (2021)
104. I. M. Pop, M. Ansmann, G. Catelani, R. J. Schoelkopf, L. I. Glazman, and M. H. Devoret, Coherent suppression of electromagnetic dissipation due to superconducting quasiparticles, *Nature* 508(7496), 7496 (2014)
105. X. Gu, A. F. Kockum, A. Miranowicz, Y. X. Liu, and F. Nori, Microwave photonics with superconducting quantum circuits, *Phys. Rep.* 718–719,1 (2017)
106. M. Reagor, H. Paik, G. Catelani, L. Sun, C. Axline, E. Holland, I. M. Pop, N. A. Masluk, T. Brecht, L. Frunzio, M. H. Devoret, L. Glazman, and R. J. Schoelkopf, Reaching 10 ms single photon lifetimes for superconducting aluminum cavities, *Appl. Phys. Lett.* 102(19), 192604 (2013)
107. M. Reagor, W. Pfaff, C. Axline, R. W. Heeres, N. Ofek, K. Sliwa, E. Holland, C. Wang, J. Blumoff, K. Chou, M. J. Hatridge, L. Frunzio, M. H. Devoret, L. Jiang, and R. J. Schoelkopf, Quantum memory with millisecond coherence in circuit QED, *Phys. Rev. B* 94(1), 014506 (2016)
108. C. Axline, M. Reagor, R. Heeres, P. Reinhold, C. Wang, K. Shain, W. Pfaff, Y. Chu, L. Frunzio, and R. J. Schoelkopf, An architecture for integrating planar and 3D cQED devices, *Appl. Phys. Lett.* 109(4), 042601 (2016)
109. J. E. Mooij, T. P. Orlando, L. Levitov, L. Tian, C. H. van der Wal, and S. Lloyd, Josephson persistent-current qubit, *Science* 285(5430), 1036 (1999)
110. C. H. van der Wal, A. C. J. ter Haar, F. K. Wilhelm, R. N. Schouten, C. J. P. M. Harmans, T. P. Orlando, S. Lloyd, and J. E. Mooij, Quantum superposition of macroscopic persistent-current states, *Science* 290(5492), 773 (2000)
111. B. Peropadre, P. Forn-Díaz, E. Solano, and J. J. García-Ripoll, Switchable ultrastrong coupling in circuit QED, *Phys. Rev. Lett.* 105(2), 023601 (2010)
112. M. S. Allman, F. Altomare, J. D. Whittaker, K. Cicak, D. Li, A. Sirois, J. Strong, J. D. Teufel, and R. W. Simmonds, RF-SQUID-mediated coherent tunable coupling between a superconducting phase qubit and a lumped-element resonator, *Phys. Rev. Lett.* 104(17), 177004 (2010)
113. M. S. Allman, J. D. Whittaker, M. Castellanos-Beltran, K. Cicak, F. da Silva, M. P. DeFeo, F. Lecocq, A. Sirois, J. D. Teufel, J. Aumentado, and R. W. Simmonds, Tunable resonant and nonresonant interactions between a phase qubit and LC resonator, *Phys. Rev. Lett.* 112(12), 123601 (2014)
114. J. Bourassa, J. M. Gambetta, A. A. Abdumalikov, O.

Astafiev, Y. Nakamura, and A. Blais, Ultrastrong coupling regime of cavity QED with phase-biased flux qubits, *Phys. Rev. A* 80(3), 032109 (2009)
115. T. P. Orlando, J. E. Mooij, L. Tian, C. H. van der Wal, L. S. Levitov, S. Lloyd, and J. J. Mazo, Superconducting persistent-current qubit, *Phys. Rev. B* 60(22), 15398 (1999)
116. Y. X. Liu, J. Q. You, L. F. Wei, C. P. Sun, and F. Nori, Optical selection rules and phase-dependent adiabatic state control in a superconducting quantum circuit, *Phys. Rev. Lett.* 95(8), 087001 (2005)
117. M. Devoret, B. Huard, R. Schoelkopf, and L. F. Cugliandolo, Quantum Machines: Measurement and Control of Engineered Quantum Systems, Oxford University Press, USA, 2014
118. V. E. Manucharyan, J. Koch, L. I. Glazman, and M. H. Devoret, Fluxonium: Single Cooper-pair circuit free of charge offsets, *Science* 326(5949), 113 (2009)
119. L. DiCarlo, J. M. Chow, J. M. Gambetta, L. S. Bishop, B. R. Johnson, D. I. Schuster, J. Majer, A. Blais, L. Frunzio, S. M. Girvin, and R. J. Schoelkopf, Demonstration of two-qubit algorithms with a superconducting quantum processor, *Nature* 460(7252), 240 (2009)
120. T. Wang, Z. Zhang, L. Xiang, Z. Jia, P. Duan, Z. Zong, Z. Sun, Z. Dong, J. Wu, Y. Yin, and G. Guo, Experimental realization of a fast controlled-Z gate via a shortcut to adiabaticity, *Phys. Rev. Appl.* 11(3), 034030 (2019)
121. A. A. Clerk, K. W. Lehnert, P. Bertet, J. R. Petta, and Y. Nakamura, Hybrid quantum systems with circuit quantum electrodynamics, *Nat. Phys.* 16(3), 257 (2020)
122. T. Niemczyk, F. Deppe, H. Huebl, E. P. Menzel, F. Hocke, M. J. Schwarz, J. J. Garcia-Ripoll, D. Zueco, T. Hümmer, E. Solano, A. Marx, and R. Gross, Circuit quantum electrodynamics in the ultrastrong-coupling regime, *Nat. Phys.* 6(10), 772 (2010)
123. A. Blais, S. M. Girvin, and W. D. Oliver, Quantum information processing and quantum optics with circuit quantum electrodynamics, *Nat. Phys.* 16(3), 247 (2020)
124. G. J. Mooney, G. A. L. White, C. D. Hill, and L. C. L. Hollenberg, Whole-device entanglement in a 65-qubit superconducting quantum computer, *Adv. Quantum Technol.* 4(10), 2100061 (2021)
125. A. Blais, R. S. Huang, A. Wallraff, S. M. Girvin, and R. J. Schoelkopf, Cavity quantum electrodynamics for superconducting electrical circuits: An architecture for quantum computation, *Phys. Rev. A* 69(6), 062320 (2004)
126. J. Clarke and F. K. Wilhelm, Superconducting quantum bits, *Nature* 453(7198), 1031 (2008)